

Mathematical Fluid Dynamics of Plasma Flow Control over High Speed Wings

Final Report
AFOSR Contract FA9550-09-C-0213

Principal Investigator:

Dr. David Marshall

Teledyne Scientific and Imaging Company
Thousand Oaks, CA 91360

Report prepared by

Dr. Alexander Fedorov and Dr. Victor Soloviev, (Co-Investigators)

Moscow Institute of Physics and Technology
Moscow, Russia

December 2010

20110207292

REPORT DOCUMENTATION PAGE*Form Approved*
OMB No. 0704-0188

Public reporting burden for this collection of information is estimated to average 1 hour per response, including the time for reviewing instructions, searching data sources, gathering and maintaining the data needed, and completing and reviewing the collection of information. Send comments regarding this burden estimate or any other aspect of this collection of information, including suggestions for reducing this burden to Washington Headquarters Service, Directorate for Information Operations and Reports, 1215 Jefferson Davis Highway, Suite 1204, Arlington, VA 22202-4302, and to the Office of Management and Budget, Paperwork Reduction Project (0704-0188) Washington, DC 20503.

PLEASE DO NOT RETURN YOUR FORM TO THE ABOVE ADDRESS.**1. REPORT DATE (DD-MM-YYYY)**

12/20/2010

2. REPORT TYPE

Final report

3. DATES COVERED (From - To)

9/30/2009 - 12/29/2010

4. TITLE AND SUBTITLE

Mathematical Fluid Dynamics of Plasma Flow Control over High Speed Wings

5a. CONTRACT NUMBER

FA9550-09-C-0213

5b. GRANT NUMBER**5c. PROGRAM ELEMENT NUMBER****5d. PROJECT NUMBER****5e. TASK NUMBER****5f. WORK UNIT NUMBER****7. PERFORMING ORGANIZATION NAME(S) AND ADDRESS(ES)**Teledyne Scientific & Imaging
1049 Camino Dos Rios
Thousand Oaks, CA 91360**8. PERFORMING ORGANIZATION**REPORT NUMBER
GO 71336**9. SPONSORING/MONITORING AGENCY NAME(S) AND ADDRESS(ES)**Air Force Office of Scientific Research
875 North Randolph Street
Arlington VA 22203-1768**10. SPONSOR/MONITOR'S ACRONYM(S)****11. SPONSORING/MONITORING
AGENCY REPORT NUMBER****12. DISTRIBUTION AVAILABILITY STATEMENT**

Approved for public release; distribution unlimited.

13. SUPPLEMENTARY NOTES**14. ABSTRACT**

This report summarizes modeling of surface dielectric barrier discharge (SDBD) and flow control. A physics-based phenomenological model was used for analytical approximations of SDBD-induced body force and heat source, which were incorporated into a Navier-Stokes solver for CFD studies. Results show that a SDBD actuator can strongly affect laminar boundary layers and that tangential jets or concentrated vortices can be generated in the near-wall flow, thus making SDBD actuators attractive for control of boundary-layer separation and laminar-turbulent transition. CFD studies of vortex flow past a delta wing at high angles of attack were carried out to estimate feasibility of flow control using SDBD actuators. Results show that for a delta wing with sharp leading edges of 60 deg. sweep angle at free-stream Mach number 1.5, the flow control strategy should focus on vortex breakdown. For actuators at the wing-apex, leading-edge, and multi-element SDBD actuators, the vortex-breakdown locus can be controlled, although the integral aerodynamic forces are weakly affected and SDBD forcing can cause unsteady oscillations of the vortex breakdown.

15. SUBJECT TERMS

Surface dielectric barrier discharge, boundary layer control, vortex breakdown control, delta wing, high angle of attack, supersonic flow, physics-based modeling, numerical studies

16. SECURITY CLASSIFICATION OF:**a. REPORT**
UNCLASSIFIED**b. ABSTRACT**
UNCLASSIFIED**c. THIS PAGE**
UNCLASSIFIED**17. LIMITATION OF
ABSTRACT**
UU**18. NUMBER
OF PAGES**
50**19a. NAME OF RESPONSIBLE PERSON**
David Marshall**19b. TELEPHONE NUMBER (Include area code)**
805-373-4170

Executive Summary

This report summarizes the efforts performed under AFOSR contracts FA9550-09-C-0213 and FA9550-07-C-0039, which constitute one project. The project includes the two major components: modeling of the surface dielectric barrier discharge (SDBD) and CFD studies SDBD flow control capabilities. The first component has been focused on developments of self-consistent theoretical models and robust computational tools providing adequate from-first-principles simulations of heat and momentum sources induced by surface discharges. The physical model and numerical code, which were developed to predict SDBD process in atmospheric air, allow us to simulate the total SDBD cycle including the discharge formation phase and the discharge relaxation phase. The predicted values of the discharge length and the surface charge density agree well with the available experimental data for positive and negative electrode polarity. This validates the developed physical model and computational code. Numerical solutions clarified basic features of the discharge evolution in space and time.

Using the numerical solutions and available experimental data we have developed a physics-based phenomenological model, which sheds light on physical processes governing the ignition and ceasing of microdischarges for the negative going half-cycle of applied alternating voltage. The obtained analytical formulae capture dependencies of the body force and discharge length on the SDBD parameters. Using the body-force values predicted by the phenomenological model and numerical results for the spatial distributions of momentum and heat sources, we have obtained analytical approximations of the SDBD-induced body force and heat source. The source terms were incorporated into Navier-Stokes solver. This computational tool has been used in the second component of the project dealing with SDBD applications to flow control.

It was shown that SDBD actuator can strongly affect the laminar boundary layer on a flat plate. Depending on distributions of applied voltage it is feasible to generate tangential jets or concentrated vortices in the near-wall flow. This flexibility and very short characteristic timescales make SDBD actuators attractive for control of viscous flows associated with the boundary-layer separation, laminar-turbulent transition or a combination of both.

CFD studies of the vortex flow past a delta wing at high angles of attack have been carried out to estimate feasibility of the vortex flow control using SDBD actuators. Computations were performed for a delta wing with sharp leading edges of 60-degree sweep angle at the free-stream Mach number 1.5. It was shown that, for this configuration, the flow control strategy should be focused on the vortex breakdown. Computations have been performed for the wing-apex SDBD, leading-edge SDBD and multi-element SDBD actuators. The heat and momentum sources produced by these actuators were symmetric with respect to the wing centerline. It was found that the vortex-burst locus can be controlled by the aforementioned actuators. Namely, the breakdown point moves downstream with the SDBD acting in the downstream direction while it moves upstream with the SDBD acting upstream. However, the integral aerodynamic forces are weakly affected. The actuator causes about 3% variations of the lift and drag coefficients. It was also shown that an asymmetric forcing, which can be produced by SDBD actuator on one side of the wing surface, triggers strong oscillations of the vortex burst loci. This, in turn, causes pulsations of the rolling moment. Because of this detrimental effect it is not clear if SDBD actuators are robust for the vortex flow control on supersonic delta wings at high angles of attack. Further numerical and experimental studies are needed to clarify this issue.

Table of Contents

<i>Executive Summary</i>	1
<i>Table of Contents</i>	2
<i>1. Background</i>	3
<i>2. Major accomplishments</i>	5
2.1 Modeling of surface dielectric barrier discharge	6
2.2 SDBD-induced momentum and heat sources	20
2.3 Boundary-layer flow control using SDBD actuator.....	20
2.4 Vortex flow over a supersonic delta wing at angles of attack	25
2.5 Vortex flow control strategy	30
2.6 Vortex flow control using symmetric SDBD forcing	31
2.7 Vortex flow control using asymmetric SDBD forcing	37
<i>3. Summary and Impact of Effort</i>	43
<i>References</i>	45
<i>Publications</i>	49

1. Background

Our original effort (2001-2003) was devoted to theoretical studies of surface discharge plasmas and other plasma devices to quench stall-slip departure due to asymmetric vortex shedding on aircraft nose tips. The application is to augment directional control/authority, agility and provide tailless capability of high-speed flight vehicles [1]. We started with theoretical modeling of vortex symmetry breaking on a sharp circular cone at high angle of attack. From slender body theory, we conceptualized a theoretical model of the vortex dynamics and estimated feasibility of vortex control by surface discharges [2]. Within the framework of an idealization of the large-scale vortex dynamics as an inviscid flow consisting of a pair of straight feeding sheets culminating in point vortices that idealize the feeding sheet rollup, we found that the symmetry breaking phenomenon is associated with nonlinear instability of a vortical singularity saddle point occurring as it rises above the body surface. Results of this effort are summarized in [2,3].

These theoretical studies were complemented by experimental effort [4,5] of the Institute of Theoretical and Applied mechanics (ITAM, Novosibirsk, Russia) that was performed under the ISTC project 2235. The experiments were conducted in ITAM's T-324 subsonic wind tunnel on a slender cone equipped with spark discharge devices. These devices created localized plasma heating that strongly displaced the cone boundary layer, triggering early separation. In accord with the theoretical predictions of [2,3], these effects stabilize the symmetric flow pattern and avoid symmetry breaking. The experiments [4,5] confirmed our concept of plasma stall-spin departure control in which primarily inviscid large-scale vortex dynamics can be controlled by spark discharge relocation of the boundary layer separation loci that are the origins of the feeding sheets. Our electromechanical system that implements this principle of viscous-inviscid boundary layer interaction control has been patented by Rockwell Scientific (RSC)-Russian team.¹ Because of the importance of the application of this technology and the need for further physics-based modeling, we have continued the previous effort with emphasis on plasma flow control actuators such as spark discharges (SD) as well as dielectric barrier discharges (DBD) that fall into a wider class of discharges known as surface barrier discharges (SBD).

In 2004-2006 we have improved the fidelity of our simulation of the viscous-inviscid interaction between the large-scale vortex dynamics and boundary layer that leads to symmetry breaking. In connection with this, a conical Navier-Stokes (CNS) approximation was applied to model vortex dynamics over a sharp cone at high angles of attack [6]. This simulation captured the symmetry breaking phenomenon. Special attention was paid to modeling of the role of turbulence in the symmetry breaking. It was shown that our CNS solver reproduces symmetric and asymmetric vortex fields and can be used for predictions of the critical angle of attack at which the vortex symmetry destabilizes. Using this tool we carried out parametric studies of surface plasma discharge effects on the vortex structure [7]. It was shown that CNS predictions are qualitatively similar to the experimental observations [4].

In connection with rapidly growing technologies relevant to flow control of high altitude flight vehicles, Dr. Norman Malmuth suggested to focus our 2007-2010 effort on plasma flow control for supersonic delta wings at high angles of attack. Similar to conical forebodies, the boundary layer globally separates from the leeward surface of delta wing at high angles of attack (α) [8].

¹Malmuth, N., Fedorov, A., Soloviev, V., Maslov, A., Zharov, V., Shalaev, I., "Surface Plasma Discharge For Controlling Forebody Vortex Asymmetry," US Pat. No. 6,796,532 (09/28/2004)

The flow field contains two strong vortices generated by the rollup of the shear layer emanating from the separation lines near the wing leading edges. Large radial and axial velocities of these vortices reduce the pressure on the wing surface under the vortex axis. This leads to increasing lift. With growing α , the lift increases nonlinearly. For sub-critical angles of attack, $\alpha < \alpha_{cr}$, the vortices are globally stable. This makes the flow field symmetrical and only weakly sensitive to flow perturbations. For supercritical angles, $\alpha > \alpha_{cr}$, the vortices exhibit a large-scale instability that is characterized by rapid deceleration and eventual stagnation of the vortex core flow as well as growth of the vortex core cross-section. These events are accompanied by strong oscillations and eventual breakdown of the vortical structure [8-10]. This phenomenon, called vortex breakdown or vortex burst, leads to a sudden decrease of the lift-to-drag ratio (L/D). If the vortex breakdown on one wing side occurs earlier than on the other, then yawing and rolling moments are induced due to flow asymmetry.

It is well known that leading-edge vortex flow is extremely sensitive to variations of surface shape and/or external forcing near the separation line. For wings with sharp leading edges, the separation line practically coincides with the leading edge. For rounded leading edges, the separation line has a complex curved shape and runs along the leading edge from the apex to the wing tip. Changing the surface boundary condition in quasi-steady state (for example, expanding surface curvature) near the separation line can cause a global change of the developing vortex [9]. Local instabilities can be also exploited for manipulations of separated vortices. As shown in [11] very small forcing can control vortex structures in the mixing layer if the forcing frequency lies within the sub-harmonic frequency band. Such forcing can be produced by plasma actuators installed near the wing leading edges (close to natural separation lines).

Plasma discharge actuators may be advantageous compared to synthetic jets, MEMS and other aerodynamic schemes. This explains the rapid growth of plasma flow control technology [12]. For this purpose, the most attractive is a surface dielectric barrier discharge (SDBD) that is of simple construction, does not change its aerodynamic shape or influence the wing when it is not in use, allows for smooth forcing frequency and power variations, and can be used for closed-loop feedback control. This motivated Corke et al. [12-14] to utilize SDBD actuators for control of boundary-layer separation near the leading edge of a subsonic airfoil at high angles of attack. The experiments [15] on a subsonic rectangular wing at the chord Reynolds numbers from of 0.35×10^6 to 0.875×10^6 demonstrated that SDBD actuators of low power (less than 250 Watts) effectively suppress leading edge separation and improve wing performance at high angles of attack.

The major gap in plasma flow control technology is the lack of self-consistent theoretical models and robust computational tools that can provide adequate simulation of heat and momentum sources induced by SDBD actuators. In contrast to numerous papers dealing with the volumetric arrangement of SDBDs, optimal surface configurations have been analyzed numerically only in a few papers such as [16,17]. Gibalov and Pietschet [16] calculated SDBD development in air for constant negative polarity electrodes. In this numerical simulation, the secondary emission of electrons from the cathode is treated as a dominant SBD mechanism, although there are experimental data showing that such discharges can be produced with no secondary emission [18]. Another shortcoming of this work (even for constant electrode polarity) is that the calculations were carried out for a relatively short time that did not cover the discharge decay phase. Accordingly, it is not feasible to compare the predicted length of the discharge region with available experimental data and validate numerical results.

The numerical simulations [17,18] addressed the more practical ease of a radio frequency (RF) surface barrier discharge. However, the modeling in [17] was performed for a diffusive discharge in helium at 300 Torr pressure when the discharge burns continuously and does not have a streamer phase, relevant to burning in air. The work in [18] simulating SBD evolution in air with an alternating voltage source has the same deficiency. The authors computed all the discharge phases with uniform time stepping that is too large to describe streamer development. Without the streamer phase, the solely diffusive model predicts gas heating and acceleration that could be physically unrealistic. Additionally, they did not account for air photoionization by UV radiation from the discharge region. This radiation is necessary for streamer production.

To bridge these gaps we have conducted combined theoretical and computation studies of SDBD physics. This allows us to identify key physical mechanisms associated with different phases of SDBD cycle and evaluate their basic parameters. Using this knowledge we have developed a self-consistent phenomenological model, which provides SDBD-induced momentum and heat sources for flow-control modeling.

2. Major accomplishments

An overview of the project effort is shown in Fig. 1. The project includes the two major components: 1) plasma discharge modeling and 2) fluid dynamics modeling.

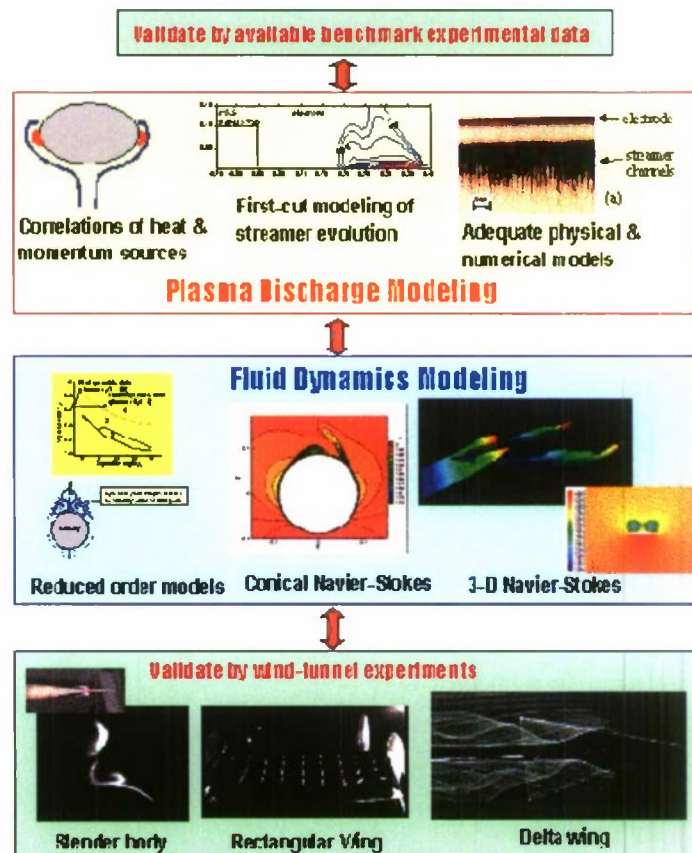


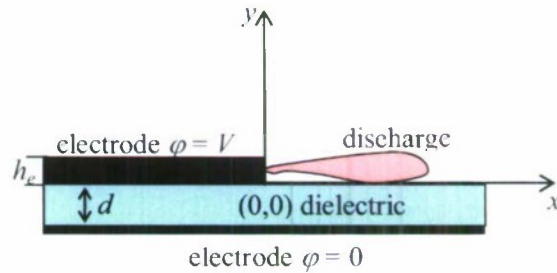
Figure 1 Project overview with major components.

The first component is focused on developments of self-consistent theoretical models and robust computational tools providing adequate from-first-principles simulation of heat and momentum sources induced by surface discharges. The second component deals with fluid dynamics modeling relevant to plasma flow control applications. These two components are strongly coupled and aimed at the development of a combined theoretical and computational toolbox for plasma flow control applications.

2.1 Modeling of surface dielectric barrier discharge

2.1.1 Accomplishments of the 2007 - 2008 effort

Schematics of SDBD electrode layout is shown in Fig. 2. The exposed electrode is assumed to be loaded by a high voltage, whereas an electrode buried under the dielectric is grounded. If the applied voltage is greater than a threshold value, the discharge starts glowing near the exposed electrode edge. According to the experimental data [16], if the exposed electrode is a cathode, then discharge takes a diffusive form. For positive exposed electrode polarity, the discharge evolves as a streamer. The discharge region length for the streamer stage is few times greater than that for the diffusive stage and in atmospheric air approximately equals to 10 mm for the near threshold voltage value $V \approx 4 - 5$ kV, the dielectric thickness $d \approx 1$ mm, and the relative dielectric permittivity $\varepsilon \approx 5 - 10$.



In the case of applied voltage of low frequency (less than 10 - 100 kHz), SDBD reveals two phases of its evolution: the discharge formation phase, when plasma layer is created due to intense air ionization, and the relaxation phase, when this plasma decays. The discharge formation phase lasts approximately 20 - 50 ns. It is accompanied by a high amplitude electrical current pulse in the external circuit. During this phase the dielectric surface is seeded by charged particles (electrons or positive ions depending on applied voltage sign), which screen the external electric field. This stops further discharge formation and its propagation along the dielectric surface. The subsequent relaxation phase lasts few microseconds, until the electric field restores its breakdown value due to both surface charge and plasma decay. Accordingly, for low frequency voltage, SDBD is arranged as a set of short (about tens of nanoseconds) current pulses separated by relatively long (few microseconds) relaxation pauses.

Figure 2 SDBD electrode layout and used coordinate system.

2.1.1a Statement of problem and governing equations

Discharge simulations have been performed in 2D approximation for the electrode layout and the coordinate system shown in Fig. 1. Hereafter the exposed semi-infinite electrode has the height $h_e = 0.1$ mm above the dielectric surface, the dielectric thickness is $d = 1$ mm, and the relative dielectric permittivity is $\varepsilon = 8$.

The model accounts for three types of charged particles: electrons, negative ions and positive ions. Their concentrations are n_e , n_- , and n_+ , respectively. The analysis of kinetic processes [19,20] showed that negative ions are primarily represented by O^- ions, and positive ions – by O_4^+, O_2^+ ions coming after a fast conversion of N_4^+, N_2^+ ions in charge-exchange collisions with O_2 molecules. Positive ions O_4^+, O_2^+ are close to equilibrium resulting only in one type of effective positive ion. The used simplified air plasma kinetic model was chosen to capture the main features of the discharge evolution, and it does not pretend to describe details of plasma composition.

The transport equations for charged particles are

$$\frac{\partial n_+}{\partial t} + \text{div} \vec{J}_+ = k_i N n_e - k_r n_+ n_- - k_{dr} n_e n_+ + S_{ph}, \quad \vec{J}_+ = n_+ K_+ \vec{E}, \quad (2.1)$$

$$\frac{\partial n_-}{\partial t} + \text{div} \vec{J}_- = 0.22 k_{at} N n_e - k_{dt} n_- N - k_r n_+ n_-, \quad \vec{J}_- = -n_- K_- \vec{E}, \quad (2.2)$$

$$\frac{\partial n_e}{\partial t} + \text{div} \vec{J}_e = S_e + S_{ph}, \quad S_e = k_i N n_e - k_{dr} n_e n_+ - 0.22 k_{at} N n_e + k_{dt} n_- N, \quad (2.3)$$

$$\vec{J}_e = -\nabla(D_e n_e) - n_e K_e \vec{E},$$

where \vec{J} = flux of particles, D = diffusion coefficient, K = mobility, the subscripts $e, +, -$ denote electrons, positive and negative ions, \vec{E} = electric field, N = air density, S_e = electron source/sink term due to ionization, recombination and attachment processes, S_{ph} = electron-ion source term due to air ionization by radiation from the discharge region. The factor 0.22 denotes an oxygen fraction in the air, k_i, k_{dr}, k_r, k_{at} and k_{dt} are rate constants for ionization, dissociative electron-ion recombination, ion-ion recombination, dissociative electron attachment and electron detachment, respectively.

The transport equations are complemented by Poisson equation for the E -field potential φ

$$\Delta \varphi = -4\pi e(n_+ - n_- - n_e) \quad \text{for gas region } (y > 0), \quad (2.4)$$

$$\Delta \varphi = 0 \quad \text{for dielectric layer } (-d < y < 0), \quad (2.5)$$

$$\mathbf{E} = -\nabla \varphi. \quad (2.6)$$

Conditions on the gas-dielectric boundary $y = 0, x > 0$ are

$$\left. \frac{\partial \varphi}{\partial x} \right|_{0+} = \left. \frac{\partial \varphi}{\partial x} \right|_{0-}, \quad \left. \frac{\partial \varphi}{\partial y} \right|_{0+} = \varepsilon \left. \frac{\partial \varphi}{\partial y} \right|_{0-} - 4\pi \sigma(x, t), \quad (2.7)$$

where $\sigma = \sigma_e + \sigma_i$ = surface charge density. Boundary conditions for the electric potential are

$$\varphi = 0 \text{ at } y = -d, \quad \varphi = V \text{ for } 0 < y < h_e, \quad x < 0, \quad (2.8)$$

$$\varphi = V \left[\frac{1}{2} - \frac{1}{\pi} \arctg \left(\frac{x}{y} \right) \right] \text{ for } y \rightarrow \infty, x \rightarrow \pm \infty, \quad (2.9)$$

where V = applied voltage (exposed electrode potential). The condition (2.9) results from an asymptotic solution of the equation $\Delta\varphi = 0$ in the semi-plane $y > 0$ with the boundary conditions (2.8) for $d \rightarrow 0$.

The rate constants are specified in Table 1, where γ = reduced electric field E/N in units of 10^{-16} V·cm². The electron temperature T_e and the ion temperature T_i are measured in Kelvin, and T_i is calculated using the Wannier expression

$$T_i = T_a + \frac{m_i + m_a}{3k_B} (K_i E)^2, \quad (2.10)$$

where T_a = gas temperature, m_i, m_a = mass of ion and N₂ molecule, k_B = Boltzmann constant.

Table 1 Ionization and sink rate constants

Reaction	Rate constant (cm ³ /s)	Reference
$e + N_2(O_2) \rightarrow 2e + N_2^+(O_2^+)$	$k_i = (0.7668 + 0.018\gamma)10^{-7.95 - \frac{38.22}{\gamma}}$	[21], [23]
$e + O_2^+ \rightarrow O + O$	$k_{dr1} = 2 \times 10^{-7} \left(\frac{300}{T_e(K)} \right)^{0.7}$	[24]
$e + O_2^+ \rightarrow O_2 + O_2$	$k_{dr2} = 1.4 \times 10^{-6} \left(\frac{300}{T_e(K)} \right)^{0.5}$	[24]
$e + O_2 \rightarrow O^- + O$	$k_{att} = 10^{-10.21 - \frac{5.7}{\gamma}}$	[21]
$O^- + N_2 \rightarrow e + N_2O$	$k_{dt} = 9.2 \cdot 10^{-13}$	[24]
$A^+ + B^+ + (M) \rightarrow A + B + M \quad (M = O_2, N_2)$	$k_r = 2 \times 10^{-6} (300/T_i)^{1.5}$	[25]

The rate constants for the processes depending on the reduced electric field E/N together with K_e , D_e , and T_e are defined by the electron energy distribution function. They are taken from Ref. [22]. The analytical approximations of these rate constants are given in Ref. [21]. The ionization rate constants and the electron drift velocity, or the electron mobility K_e , are further corrected to fit the data [23] (this has been discussed in Refs. [19, 20]). Finally, the following expressions for K_e , T_e , and D_e have been used

$$K_e \left(\frac{\text{cm}^2}{\text{V} \cdot \text{s}} \right) = \begin{cases} 866 & \gamma < 1 \\ 383 \cdot (1 + 1.262/\gamma) & 1 < \gamma < 20 \\ 275 \cdot (1 + 9.6/\gamma) & \gamma > 20 \end{cases}, \quad (2.11)$$

$$T_e(K) = \begin{cases} T_a + 8645 \cdot \gamma^{0.54069} & \gamma < 1 \\ T_a + 8645 \cdot \gamma^{0.4} & \gamma > 1 \end{cases}, \quad (2.12)$$

$$D_e = \frac{k_B T_e K_e}{e}. \quad (2.13)$$

The mobility of O_2^+ and O_4^+ ions in atmospheric air is known to be 2.4 and 2.05 cm²/Vs, respectively. We imply $K_+ = 2.1$ cm²/Vs for effective positive ions and $K_- = 3.2$ cm²/Vs for negative O^- ions. The electron-ion recombination and electron detachment rate constants are taken from Ref. [24], and the ion-ion recombination rate constant is taken from Ref. [25].

In the right-hand sides of Eqs. (2.1) and (2.3), the source term S_{ph} is due to the photo-ionization of O_2 molecules by UV radiation of $N_2(b^1\Pi_u, b^1\Sigma_u^+, c^1\Sigma_u^+)$ excited molecules in the band 98.0-102.5 nm. This source term was discussed and deduced in Ref. [26] and its expression for 2D case has been obtained in Refs. [19,20]

$$S_{ph}(x, y) = \frac{Q_{ph} N_{O_2} N_{\alpha_{ex}} \tau^*}{2\pi\tau_R} \int_{-\infty}^{\infty} \int_0^{\infty} n_e(x_a, y_a) k_i(x_a, y_a) \exp(-Q_{ph} N_{O_2} \rho_a) \arctan\left(\frac{h_{str}}{2\rho_a}\right) \frac{dx_a dy_a}{\rho_a}, \quad (2.14)$$

$$\rho_a = \sqrt{(x - x_a)^2 + (y - y_a)^2}.$$

Here $Q_{ph} = 1.4 \times 10^{-17}$ cm² is an average over the absorption band photo-ionization cross section of O_2 molecules, $N_{O_2} = 0.22N$ is O_2 molecules concentration in air, $\alpha_{ex} = 0.07$ is a ratio of excitation rate of N_2 molecules by electron impact to their ionization rate, $\tau^* / \tau_R = (25.33N / N_0 + 1)^{-1}$ is a ratio of the total lifetime of excited molecule $N_2(b^1\Pi_u, b^1\Sigma_u^+, c^1\Sigma_u^+)$ to its radiative lifetime, and $h_{str} \approx 0.1$ mm is the characteristic size of streamer head.

For dimensionless presentation of the results we use the scaling parameters: $n_0 = 0.82 \times 10^{12}$ cm⁻³ for charged particle densities, $E_0 = 40.35$ kV/cm for electric field, and $\varphi_0 = 1.091$ kV for potential. The ionization threshold electric field in atmospheric air is $E_{th} = 32.28$ kV/cm.

2.1.1b Initial and boundary conditions for transport equations

Because the diffusion flux of ions is 4-5 orders of magnitude smaller than their drift flux, it can be neglected everywhere, even at the discharge front. Hence the electron transport equation is parabolic, and the ion transport equations become hyperbolic without diffusion flux. In accord to the type of equations, the boundary conditions read

$$n_+ = n_e = n_- = 0, \text{ if } y \rightarrow \infty, \text{ or } x \rightarrow \pm \infty, \quad (2.15)$$

for charged particle concentrations at infinity;

$$n_+ = n_- = 0, \text{ if } y = h_e, \ x < 0, \quad (2.16)$$

for positive and negative ion concentrations at the electrode surface;

$$n_+ = 0, \text{ if } y = 0, \ x > 0, \text{ and } E_y > 0, \quad (2.17)$$

for positive ion concentrations at the dielectric surface, when the ion flux is directed outward the surface. For negative ion concentration the similar condition reads

$$n_- = 0, \text{ if } y = 0, \ x > 0, \text{ and } E_y < 0. \quad (2.18)$$

For electrons, we use a general boundary condition coming from ab initio physics and valid for any surface. This condition expresses the hydrodynamic flux near the surface via the kinetic flux and reads

$$-K_e n_e E_y - \frac{\partial(D_e n_e)}{\partial y} = -a(E_y) \frac{n_e V_T}{4} + f_{out}, \quad \text{for } y=0, x>0 \text{ and } y=h_e, x<0, \quad (2.19)$$

where

$$a(E_y) = \begin{cases} (1-r) \exp\left(\frac{K_e E_y \lambda}{T_e}\right) & \text{for } E_y < 0 \\ (1-r) \left[\exp\left(-\frac{K_e E_y \lambda}{T_e}\right) + 4 \left(1 - \exp\left(-\frac{K_e E_y \lambda}{T_e}\right)\right) \right] & \text{for } E_y > 0 \end{cases}, \quad (2.20)$$

$$f_{out} = \begin{cases} -\gamma_s J_{iy} & \text{if } y = h_e, x < 0, E_y < 0 \\ 0 & \text{if } y = 0, x > 0 \end{cases}. \quad (2.21)$$

Here V_T = electron thermal velocity, λ = electron mean free path, r = surface reflection coefficient for electrons (hereafter it is assumed that $r = 0$), γ_s = electron secondary emission coefficient, f_{out} = electron flux from the surface ($f_{out} = 0$ for the dielectric surface and the anode electrode, and $f_{out} = -\gamma_s J_{iy}$ for the cathode electrode).

The electron secondary emission coefficient γ_s depends on electrode material and applied voltage. Usually it is of the order of 0.01 – 0.1 [27]. We assume that $\gamma_s = 0$, because our computations showed that results do not notably depend on this parameter.

The balance equations for the surface density of electrons, σ_e , and ions, σ_i , read

$$\frac{\partial \sigma_e}{\partial t} = -J_{ex}, \quad \frac{\partial \sigma_i}{\partial t} = -J_{ix}. \quad (2.22)$$

The initial conditions are

$$n_i = n_e = n_{im}, \quad n_- = 0, \quad \sigma_i(x, 0) = \sigma_e(x, 0) = 0 \text{ at } t = 0, \quad (2.23)$$

where n_{im} = background concentration of electrons and positive ions. Hereafter we use $n_{im} = 10^8 \text{ cm}^{-3}$. This parameter affects only the initial delay time of the discharge formation and does not affect the discharge evolution.

2.1.1c Numerical algorithm and refinement of ionization source

Because of a steep electric field and electron-ion density gradients relevant to ionization wave front in the case of streamer formation and to cathode layer structure in the case of negative exposed electrode polarity, the spatial size of computational cell should be less than 0.002 mm. This mesh was used for calculations discussed hereafter. Transport equations were solved using an implicit numerical algorithm with “upwind” approximation for the electron drift flux and Gauss elimination (sweep) technique for the electron diffusion. To resolve a strong nonlinearity due to the ionization source in the right-hand side of Eqs. (2.1) and (2.3), an iteration procedure was applied. Relative accuracy of iterations was 0.01. The Poisson equation for the self-

consistent electric field potential was solved using the improved Gauss-Seidel (upper relaxation) method with relative accuracy 10^{-5} .

If the E -field is strongly inhomogeneous in space, then the ionization rate constant should be obtained by solving the inhomogeneous Boltzmann kinetic equation. Nevertheless, a reasonable estimate of this rate constant can be made using the energy conservation equation for electrons. Our theoretical analysis gives the following expression for the ionization rate constant, which is corrected to account for the non-local ionization,

$$k_{i, \text{nl}} = k_i \left(1 + \frac{\vec{E} \nabla (D_e n_e)}{K_i n_e E^2} \right). \quad (2.24)$$

The new model comprising the ionization rate constant (2.24) allow us to simulate the discharge evolution from the beginning to the time instant when the discharge stops propagating along the dielectric surface. This was demonstrated for both negative and positive electrode polarities.

2.1.1d Results and discussion

The physical and numerical model for SDBD in atmospheric air has been developed accounting for air photoionization by UV radiation from discharge zone, approximation of non-local ionization source and universal boundary conditions on the electrode and dielectric surfaces. The refined model and new computational code allow for simulations of the total SDBD cycle including both the discharge formation and the discharge relaxation phase.

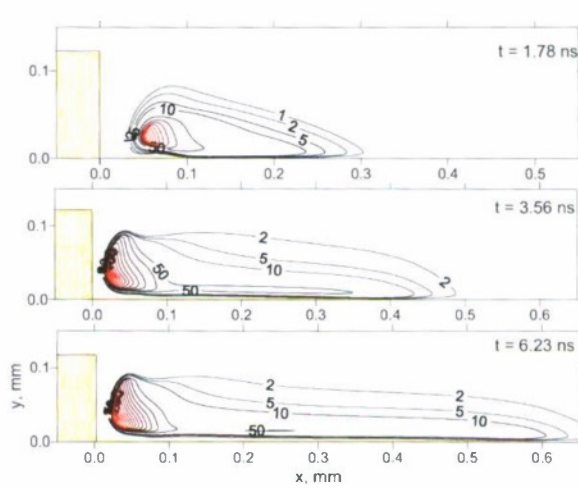


Figure 3 Electron density n_e/n_0 contours evolution at $V = -4.5$ kV, rectangular region denotes the exposed electrode.

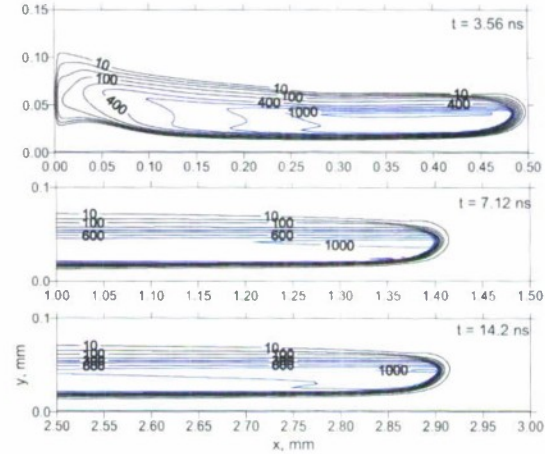


Figure 4 Streamer evolution predicted by the developed model; electron density n_e/n_0 contours for $V = +4.2$ kV.

The discharge formation phase lasts few tens of nanoseconds and creates plasma. The discharge evolves as a streamer for positive electrode polarity (Fig. 4) and as a diffusive discharge with a narrow cathode region for negative electrode polarity (Fig. 3). The predicted values of the discharge length and the surface charge density agree well with available experimental data for positive and negative electrode polarities (Figs. 5 and 6). This validates the developed physical

model and computational code. Although the discharge formation phase gives negligible contribution to the momentum and heat sources relevant to flow control applications, it provides the initial conditions for the relaxation phase.

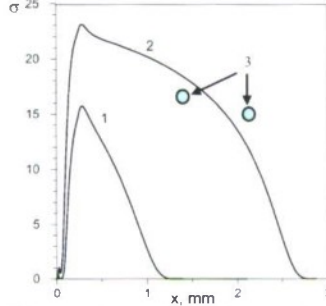


Figure 5 Surface charge density σ in units of nC/cm^2 for simulated streamer evolution; (1) – $t = 7.12 \text{ ns}$, (2) – $t = 14.2 \text{ ns}$, (3) – experiment [16]; $V = +4.2 \text{ kV}$.

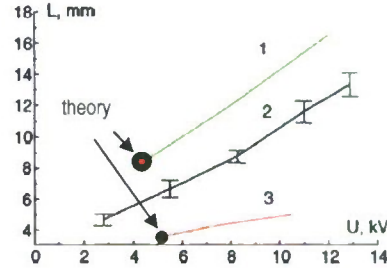


Figure 6 Experimentally observed SDBD length [16]: (1) – constant voltage $U > 0$, (2) – alternating voltage, (3) – constant voltage $U < 0$. Symbols show predictions of the developed model at $V = +4.2 \text{ kV}$ and $V = -5 \text{ kV}$ ($V \equiv U$).

The relaxation phase begins when plasma is redistributed in such a way that it shields the external electric field and reduces the air ionization rate in the discharge region to very small value. The ion-electron and ion-ion recombination along with the ion drift motion are main processes in the relaxation phase which lasts few microseconds. This phase effectively contributes to the momentum and heat sources relevant to flow control applications.

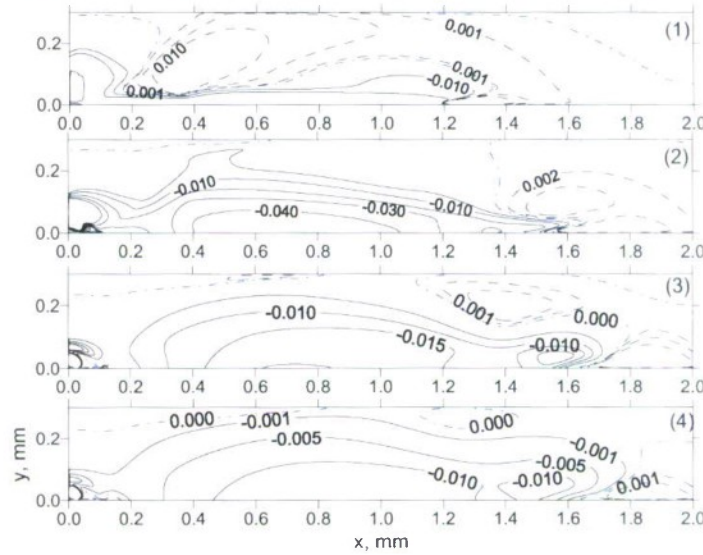


Figure 7 Contours of time averaged momentum source x-component in units of 10^7 N/m^3 for SDBD relaxation at $V = -5 \text{ kV}$: (1) – $t = 0.18$, (2) – 0.62 , (3) – 1.1 , (4) – $1.8 \mu\text{s}$.

The spatial distribution of charged particles and their composition are quite different in the discharge formation phases and the discharge relaxation phase. During the discharge formation,

plasma occupies a thin near-surface layer of ≈ 0.05 mm thickness for positive electrode polarity (streamer discharge) and ≈ 0.02 mm thickness for negative electrode polarity (diffusive discharge). In the relaxation phase, plasma spreads outward the dielectric surface, and the thickness of momentum-source layer increases to ≈ 0.3 mm at both positive and negative electrode polarities. For a case of streamer relaxation at decreasing applied voltage, the thickness of heat-source layer is approximately 2 times smaller (≈ 0.1 mm), and for negative electrode polarity it is close to the thickness of momentum-source layer.

The momentum-source distributions have a complicated structure in space. For positive electrode polarity, the length of positive force region is approximately 0.3-1.0 mm. For negative electrode polarity, the body force is an order of magnitude greater than in the case of positive applied voltage (its absolute value achieves 10^5 N/m³ as shown in Fig. 7).

2.1.2 Accomplishments of the 2010 effort

The model developed in 2007-2008 allows us to simulate the building up and relaxation of a single microdischarge only. The obtained data are not sufficient to predict the momentum and heat sources induced by actual DBD-plasma actuators. These sources result from few tens of consequent microdischarges developed during each half-period of alternating applied voltage. Because numerical modeling of this bulk of microdischarges is extremely time-consuming, the problem has not been solved yet except for the case of negative ramp voltage [6].

In 2010 we tried to estimate the momentum and heat sources induced by SDBD using a phenomenological model of discharge action on the quiescent air based on existing experimental data and achieved understanding of SDBD physics [28,29]. The primary objective of this work is to obtain analytical approximations of the body force and discharge length in order to recognize main trends of their dependences on applied voltage parameters and dielectric material properties and understand how to improve the SDBD flow control performance.

2.1.2a Phenomenological model of SDBD induced body force

The body force generated by a surface dielectric barrier discharge is due to momentum transfer from electrons and ions to neutral gas molecules [30]

$$\mathbf{F} = e(n_p - n_n - n_e)\mathbf{E}. \quad (2.25)$$

Here e = electron charge, n_e, n_p, n_n = densities of electrons, positive and negative ions, respectively, and E = electric field strength. According to Eq. (2.25) the body force is proportional to self-consistent E -field value and positive or negative charge density surplus.

Electrons and ions are produced during the building up of microdischarge, which lasts few tens of nanoseconds. Then, between the consequent microdischarges, they recombine, convert to another type of ions and/or move to the dielectric surface leaving the gas volume. This relaxation phase is characterized by a microsecond time scale. The electrical charge generated in a microdischarge due to air ionization is divided into three parts. The charges of sign that is opposite to electrode potential sign move to electrode and form conductivity current in the external electrical circuit. The charges of the same sign as the sign of electrode potential drift out

of the electrode and form both the surface charge layer on the dielectric surface and volumetric charge. These charges screen the external electric field and lead to the microdischarge end off.

Inside a microdischarge series, which is relevant to the voltage half-cycle of constant polarity, the charges having the opposite to electrode polarity sign are not delivered to the surface. Accordingly, no charge recombination occurs on the surface during the microdischarge series, and the surface-charge relaxation time is much greater than the half period of applied voltage. This means that the recovery of breakdown condition and repetition of microdischarges in a microsecond scale observed in experiments is possible only due to the increase of applied voltage and not due to the decrease of surface charge.

Numerical simulations [28] of a set of microdischarges at a ramp voltage showed that at the beginning of the microdischarge series the time interval between the neighbor microdischarges is inversely proportional to the voltage slope: $\Delta\tau_{md} \sim \left(\frac{dV}{dt}\right)^{-1} \sim \frac{1}{V_0 f_v}$, where V_0 = voltage amplitude and f_v = voltage frequency. The number of microdischarges in a series is

$$N_{md} \approx \frac{T_v(V_0 - V_{bd})}{2\Delta\tau_{md}V_0}, \quad N_{md} \sim (V_0 - V_{bd}), \quad (2.26)$$

where V_{bd} = breakdown voltage for the first microdischarge, and $T_v = f_v^{-1}$ is period of applied voltage.

The number of microdischarges is proportional to the difference between the voltage amplitude and the breakdown voltage and may be determined as

$$N_{md}(t) = \frac{V(t) - V_{bd}}{\delta V}, \quad (2.27)$$

where δV is the voltage increase, which is necessary to recover the breakdown condition for igniting a new microdischarge. The relation between δV and $\Delta\tau_{md}$ is $\Delta\tau_{md} = \frac{T_v \delta V}{2V_0}$.

The volumetric charge created in a microdischarge has an opposite to electrode potential sign. Therefore, the body force, which is averaged over time and integrated over space, is positive (directed out of the electrode edge) both for positive and negative electrode polarity. This was shown by straight and time resolved body force measurements [31-34]. Following the commonly used notation [31] we call the discharge at a negative going potential half cycle as a forward stroke and the discharge at a positive going potential half cycle as a backward stroke.

The volumetric charge surplus leaves the volume due to drift onto the dielectric surface in tangential direction (along the dielectric surface), because the normal component of electric field has been screened by surface charge at the stage of microdischarge building up. The volumetric charge in air is primarily presented by molecular ions. In the case of forward stroke, when electrons start to form the volumetric charge, it is due to rapid electron attachment to oxygen molecules and rapid conversion of atomic ions O into molecular ions O_2 [20]. In the case of backward stroke, the molecular ion structure of volumetric charge is natural because positive molecular ions are created due to air ionization and further they just change their composition in ion conversion reactions [20]. Hence the relaxation time of the volumetric charge may be

estimated as the drift time of molecular ions along the dielectric surface: $\Delta\tau_q \approx L / v_{dr_{-i}}$, where $v_{dr_{-i}}$ = ion drift velocity. According to the numerical simulation [29] the average E -field for microdischarge decaying air plasma is around 5 kV/cm, the ion mobility approximately equals 2-3 cm²/(Vs). This gives $v_{dr_{-i}} \approx 10^4$ cm/s.

The discharge length L depends on the applied voltage amplitude V_0 , the dielectric thickness d and the dielectric relative permittivity ε [16]. As a reference point we consider $V_0 \approx 10$ kV, $d \approx 1$ mm, $\varepsilon \approx 5-10$. For this conditions, $L \approx 10$ mm [16] and $\Delta\tau_q \approx 100 \mu s$. The experimentally observed time interval between microdischarges is primarily governed by the voltage increase, and it is $\Delta\tau_{md} \approx 15 \mu s$. Accordingly, the volumetric charge relaxation time $\Delta\tau_q$ is much greater than the time interval between microdischarges, $\Delta\tau_q \gg \Delta\tau_{md}$. Relaxation of the volumetric charge mainly occurs after the end of a microdischarge series, when the voltage slope changes its sign. Hence the volumetric charge accumulates during the development of microdischarge series, and the body force induced by this increasing charge grows during the voltage half cycle. For the forward stroke, accumulation of the negative volumetric charge has been modeled numerically in Ref. [28]. The force increase during the voltage half cycle has been demonstrated experimentally in Refs. [33,34] for forward and backward strokes.

The accumulated volumetric charge is proportional to the number N_{md} of microdischarges in a series. For normal SDBD developments, this number remains constant for the constant voltage amplitude and does not depend on the voltage frequency (see Eq. (2.26)). In this case, a set of microdischarges ends off when the voltage achieves its amplitude value V_0 , and the voltage slope changes its sign [16,31].

The N_{md} and corresponding surface and volumetric charges increase with V_0 until they reach saturation levels. We suppose that this occurs when the volumetric charge, which is accumulated in a microdischarge series, becomes high enough to contribute into the external voltage screening in the same extent as the surface charge. If the saturation is achieved, the set of microdischarges ends off before the voltage reaches its amplitude value. The corresponding current signal of microdischarge series was observed experimentally [35]. The maximal body force was observed for the maximal volumetric charge, and N_{md} was reached at the saturation point.

Because of great difference between the characteristic gasdynamic time $\tau_g \sim L / U_\infty \sim 10^{-3} - 10^{-4}$ s and the microdischarge evolution time $\sim 10^{-6}$ s (L is the discharge length, and U_∞ is the free-stream velocity), the momentum and heat sources averaged over the alternating voltage cycle are relevant to aerodynamic forcing. The body force, averaged over the voltage cycle, includes integration of the instantaneous force over the forward and backward strokes

$$\bar{F} = \frac{1}{T_V} \int_0^{T_V/2} F_+(t) dt + \frac{1}{T_V} \int_{T_V/2}^{T_V} F_-(t) dt .$$

According to theoretical predictions for a single microdischarge evolution [29], the backward stroke force $F_-(t)$ should be an order of magnitude smaller than the forward stroke force $F_+(t)$. This is because of quite different plasma and electric field spatial distributions generated at positive and negative electrode polarity (see Section 2.1.1). In the experiments [33,34], the body

force were approximately the same for the forward and backward strokes. These measurements provided an average (over the exposed electrode length) force. The recent experiment [32] showed that the body-force spatial distribution along the electrode length is extremely inhomogeneous. Generally, the body force for the negative going voltage half-cycle is much greater than that for the positive going voltage half-cycle. But at some points on the electrode edge the reverse ratio takes place. Forgoing means that the correct estimation of the body force value could be made by accounting for the forward stroke force only. The backward stroke force contribution may either be negligible or increase the result not more than by factor 2.

2.1.2b Body force estimation for negative going voltage

Consider the SDBD evolution at a normal regime far from the saturation limit. For negative electrode polarity, the microdischarge process is similar to that observed in a glow discharge [29]. The cathode layer is formed after air breakdown in the vicinity of the exposed electrode edge. Electron-ion generation due to air ionization occurs primarily inside this cathode layer. The ions are moved to the cathode by strong electric field, and electrons drift in the opposite direction towards the dielectric surface. Assume that each microdischarge generates approximately the same amount of electrons possessing a charge Δq . The main part of these electrons rapidly leaves the discharge volume reaching the dielectric surface, and the rest part is converted into negative O_2^- ions due to attachment to O_2 molecules [20] creating a volumetric charge Δq_n of negative ions.

The probability of the negative ion formation on electron drift way to dielectric surface is estimated as $p_n(t) \approx \frac{\nu_{at} l(t)}{K_e E_{xt}(t)}$, where ν_{at} = attachment frequency of electron to O_2 molecule, $l(t)$ = current value of the surface charge length (discharge length), K_e = electron mobility, and $E_{xt}(t)$ = current value of electric field tangential component above the surface charge layer. Electrons drift in the tangential direction because the normal electric field component equals to zero due to the surface charge screening. The surface charge layer length is

$$l(t) \approx \frac{4\pi d \Delta q N_{ind}(t)}{\varepsilon V_s(t)}, \quad L = \max(l(t)), \quad (2.28)$$

where V_s = average potential of the dielectric surface at a surface charge location. The negative ion residence time inside a volume is estimated as $\Delta\tau_n \approx \frac{l(t)}{K_n E_{xt}(t)}$, where K_n = negative ion mobility.

Estimation of the time averaged body force inside a microdischarge series reads

$$\bar{F} \approx \frac{1}{T_v} \int_0^{T_v} q_n(t) E_{xt}(t) dt. \quad (2.29)$$

Following available experimental data we assume that $N_{ind}(t)$ and $l(t)$ are proportional to t , the current value of accumulated volumetric charge is expressed as

$$q_n(t) \approx \frac{1}{3} N_{md}(t) \cdot \Delta q \cdot p_n(t). \quad (2.30)$$

Then

$$\bar{F} \approx \frac{1}{3T_v} \int_0^{T_v} N_{md}(t) \Delta q \frac{\nu_{nl} l(t)}{K_e} dt. \quad (2.31)$$

Integration in Eq.(2.31) finally gives the body force

$$\bar{F} \approx \frac{\nu_{nl} L^2 N_{md} f_v \Delta q}{3K_e K_n E_{dl}}. \quad (2.32)$$

Equation (2.32) is valid for $f_v \Delta \tau_n < 1/2$. More correct expression, which accounts for the body force decrease for $f_v \Delta \tau_n > 1/2$, is

$$\bar{F} \approx \frac{\nu_{nl} L N_{md} \Delta q}{3K_e} \exp(-f_v \Delta \tau_n) [1 - \exp(-f_v \Delta \tau_n)]. \quad (2.33)$$

The experiments [32] show that all microdischarges in a series are started from the exposed electrode edge and not from the edge of the surface charge layer created by previous microdischarges. Hence, in order to estimate Δq , N_{md} and L , we have considered an asymptotic analytical solution for electric field near the electrode edge. The air breakdown condition reads [27]

$$\int_{C_E} \alpha_T(r) dr = \ln(1 + \gamma^{-1}), \quad (2.34)$$

where the Townsend coefficient α_T is integrated along the line of E -field C_E from the electrode edge to the dielectric surface, and γ = coefficient of secondary electron emission from the cathode surface. A semi-empirical expression of α_T for the air is $\alpha_T = A p \exp(-B p / E)$, where $A = 15 \text{ cm}^{-1} \text{ Torr}^{-1}$, $B = 365 \text{ V cm}^{-1} \text{ Torr}^{-1}$, and p = air pressure in Torr [27].

The breakdown condition (2.34), with substitution of the aforementioned E -field near the electrode edge after appropriate analysis and calculations, gives the breakdown voltage

$$V_{bd} \approx \pi B \sqrt{\frac{p d \ln(1 + \gamma^{-1})}{2A}}. \quad (2.35)$$

The E -field contours C_E satisfying the condition (2.34) are ended on the dielectric surface at some distance from the electrode edge. Hence the surface charge layer, which is created by drifting to dielectric surface electrons, does not flank to the electrode edge. Numerical simulation shows that the distance l_{bd} between the electrode edge and the starting point of surface-charge layer is about $d/2$. Hereafter we use $l_{bd} \approx d/2$.

To get the voltage increase δV , which is necessary to compensate the screening effect of the surface charge and restore the breakdown condition, we have analytically estimated the electric field inside the gap between the electrode edge and the surface charge layer. By variation of the air breakdown condition in the gap we obtain

$$\delta V(\text{kV}) \approx 2d(\text{cm}), \text{kV}. \quad (2.36)$$

Using the foregoing estimates of δV , V_{bd} , E_{xl} , N_{md} and Δq , the discharge length and the body force are evaluated as

$$L(\text{cm}) \approx 0.1 \cdot V_0(\text{kV}) \left(1 - \frac{V_{bd}}{V_0} \right), \quad (2.37)$$

$$\bar{F}(\text{N/m}) \approx 10^{-7} \frac{f_v(\text{kHz})}{d(\text{cm})} V_0^4(\text{kV}) \left(1 - \frac{V_{bd}}{V_0} \right)^4. \quad (2.38)$$

Figure 8 shows that the theoretical estimate (2.38) agrees satisfactorily with the experimental data [36] for dielectric layers of different materials and thickness. Some disagreement for near breakdown voltages can be attributed to the inaccuracy of the breakdown voltage estimation because of inaccuracy of the used asymptotic E -field value near the electrode edge.

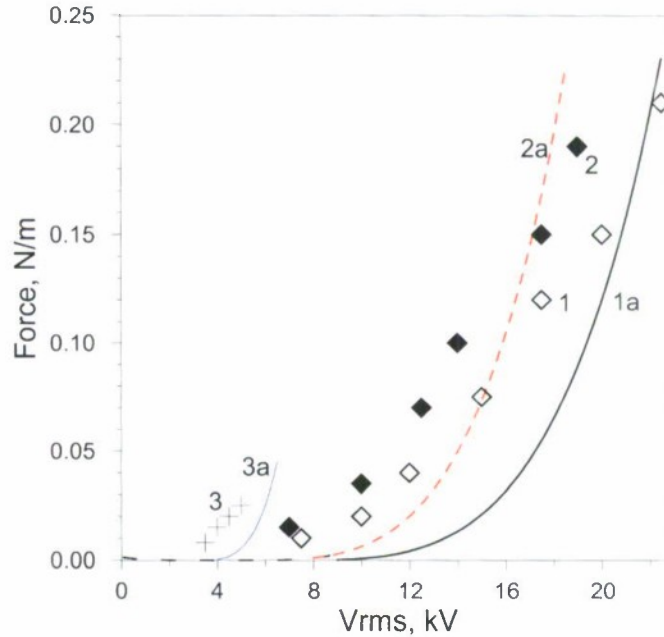


Figure 8 Theoretical estimations of the body force (lines) against the experimental data [36] (symbols) for 1,1a – teflon ($\epsilon=2$), $d = 6.35\text{mm}$, $f_v=2.1\text{kHz}$; 2,2a – teflon, $d = 3.18\text{ mm}$, $f_v=2\text{ kHz}$; 3,3a – kapton ($\epsilon=3.9$), $d = 0.15\text{ mm}$, $f_v=4.4\text{kHz}$.

2.1.2c Discussion

The developed phenomenological model sheds light on physical processes governing the ignition and ceasing of microdischarges for the negative going half-cycle of applied alternating voltage. This model clarifies reasons of the body force saturation observed in experiments. The obtained

analytical formulae capture basic dependencies of the body force and discharge length on the applied voltage parameters, dielectric thickness d and its relative permittivity ϵ . The model is validated against the experimental data providing the body force variation versus voltage amplitude for different dielectric materials and their thicknesses.

For negative electrode polarity, a gap between the exposed electrode edge and the surface charge layer provides an easy start for consequent microdischarges. Because the electric field inside this gap remains rather high, even when a microdischarge ends off and relaxes, a small increase of applied voltage is sufficient to restore the air breakdown condition and start a new microdischarge. This voltage addition primarily depends on the dielectric thickness d , while it is weakly affected by the voltage value and ϵ . The number of microdischarges during the voltage half-cycle is proportional to the voltage amplitude and does not depend on the voltage frequency. Hence the time interval between microdischarges is inversely proportional to the voltage amplitude and its frequency.

For negative going voltage, the discharge length is proportional to the voltage amplitude and practically does not depend on d and ϵ . This result looks surprising because the experimentally observed discharge length for alternating voltage decreases with ϵ [16]. This could be explained by the fact that the discharge length is much greater for the positive going voltage half-cycle. Accordingly, for alternating voltage, its dependence on ϵ is associated with the discharge length at positive going voltage. Additional experiments are needed to clarify this issue.

The proposed model captures experimental dependencies of the body force on voltage at different d and ϵ . This indicates that the volumetric force is primarily induced by the negative going voltage half-cycle. The force associated with the positive going voltage half-cycle should not change the result significantly.

The body force is due to accumulation of the volumetric negative charge carried by negative long-lived O_2^- and O_3^- ions. This accumulation is proportional to L^3 giving a strong dependence of the body force on applied voltage. The probability of negative ion formation due to electron attachment is proportional to L^2 and the residence time of negative ion in the volume is also proportional to L^2 .

To increase the force and improve the SDBD actuator performance, one has to increase the volumetric charge of negative ions. This could be achieved by artificial increasing of the discharge length. The latter can be done by shifting the encapsulated electrode downstream of the exposed electrode or by using a dielectric of small conductivity.

The idea to use a "conducting" dielectric was proposed and tested in Princeton two years ago [37]. They could not improve the actuator performance. The reason of this failure may be due to the fact that they have used nanosecond pulses instead of a sinusoidal voltage of moderate frequency. They tried to decrease the surface charge in the time scale between the pulses preventing the negative ion accumulation. To get a positive effect one should use a sinusoidal voltage (supporting a microdischarge series and negative ion accumulation) and supply the time of surface charge reduction due to finite dielectric conductivity close to the voltage period. For the material used in experiment [37] (linen based phenolic) this time corresponds to frequency of applied voltage ~ 1 kHz. It is expected that further studies of this problem can lead to significant improvements of the SDBD performance.

2.2 SDBD-induced momentum and heat sources

Using the body-force absolute values predicted by the developed phenomenological model and numerical results for the spatial distributions of momentum and heat sources, we obtain analytical approximations of the volumetric force components (F_x, F_y) and the heat source Q

$$F_x(x, y, t) = \varphi(t)F_{xd}(x, y),$$

$$F_y(x, y, t) = \varphi(t)F_{yd}(x, y),$$

$$Q(x, y, t) = \varphi(t)Q_d(x, y),$$

where

$$F_{xd} = A_{xd}g_d(x)f(y), F_{yd} = A_{yd}g_d(x)f(y), Q_d = A_{qd}g_d(x)f(y). \quad (2.39)$$

The functions $g_d(x)$, $f(y)$ and $f_q(y)$ are expressed as

$$g_d(x) = \left[1 - \left(\frac{x - x_1}{l_d} \right)^2 \right]^{10.2}, \quad x_1 \leq x \leq x_2,$$

$$f(y) = A_f y \exp \left[-\frac{\sigma_f (y - h_d)^2}{2} \right], \quad A_f = 7547 \text{ m}^{-1}, \sigma_f = 10^8 \text{ m}^{-2},$$

$$f_q(y) = A_q y \exp \left[-\frac{\sigma_q (y - h_w)^2}{2} \right], \quad A_q = 3 \cdot 10^4 \text{ m}^{-1}, \sigma_q = 4 \cdot 10^8 \text{ m}^{-2},$$

where $l_d = 5 \text{ mm}$ is the discharge length, $h_d = 0.1 \text{ mm}$ and $h_w = 0.005 \text{ mm}$ are vertical sizes of the discharge region, $x_1 = 2.5 \text{ cm}$, $x_2 = x_1 + l_d$. The $\varphi(t)$ is a step-function: $\varphi(t) = 0$ for $t \leq 0$, $\varphi(t) = 1$ for $t > 0$. The constants in Eq. (2.39) are

$$A_{xd} = \pm 10^5 \text{ N/m}^3, A_{yd} = -2 \cdot 10^4 \text{ N/m}^3, A_{qd} = 10^7 \text{ W/m}^3.$$

Plus (or minus) in the expression for A_{xd} correspond to the upstream (or downstream) shift of the exposed electrode with respect to the buried electrode.

2.3 Boundary-layer flow control using SDBD actuator

To shed light on aerodynamic effects produced by SDBD actuator, we consider a relatively simple flow – the laminar boundary layer on a flat plate in a free stream of low subsonic speed. The plate has zero thickness and sharp leading and trailing edges. The computational domain and Cartesian coordinate system are shown in Fig. 9. Part of the bottom boundary corresponds to the plate surface $0 \leq x \leq 0.1 \text{ m}$. The inlet boundary is located at $x = -0.05 \text{ m}$, and the outlet boundary is located at $x = 0.2 \text{ m}$. The 2D SDBD forcing is produced in the region $0.025 \text{ m} \leq x \leq 0.031 \text{ m}$. The computational grid has approximately 210,000 hexahedral cells:

300 grid nodes are in the boundary-layer region in the vertical direction, and 580 grid nodes are along the plate surface. Clustering of the grid nodes is used in the vicinity of SDBD actuator, $0.020 \text{ m} \leq x \leq 0.050 \text{ m}$.

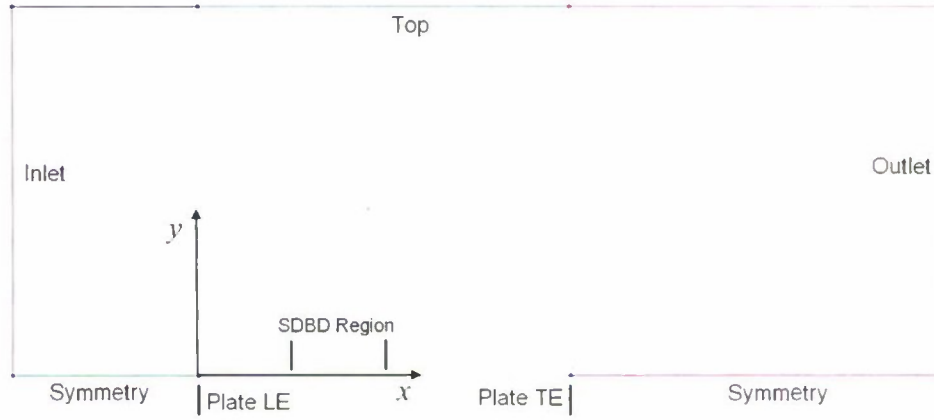


Figure 9 Computational domain and coordinate system.

Although the flow has small subsonic speeds, the gas compressibility is taken into account to simulate effects of the SDBD-induced heat source. 2D unsteady Navier-Stokes equations are integrated using an implicit second-order finite-volume method. The governing equations are approximated by a conservative scheme. The viscosity-temperature dependence is calculated using the Sutherland law with constant 110.4K. The fluid is a perfect gas having the specific heat ratio $\gamma = 1.4$ and Prandtl number $Pr = 0.72$.

The freestream parameters are: velocity $U_\infty = 10 \text{ m/s}$, pressure $p_\infty = 10^5 \text{ Pa}$; density $\rho_\infty = 1.2 \text{ kg/m}^3$, temperature $T_\infty = 290 \text{ K}$, the Reynolds number is $Re_\infty = \rho_\infty U_\infty x_1 / \mu_\infty = 1.73 \times 10^4$, where $x_1 = 0.025 \text{ m}$ is the SDBD leading edge coordinate, which is chosen so that the boundary layer thickness is $\delta(x_1) \approx 1 \text{ mm}$.

The freestream conditions are imposed on the inlet and top boundaries. On the outlet boundary, a linear extrapolation of dependent variables is used. The boundary conditions on the bottom boundary are: the flow symmetry condition upstream from the plate leading edge and downstream from the plate trailing edge; no-slip condition and the adiabatic wall temperature on the plate surface.

2.3.1 Steady SDBD forcing

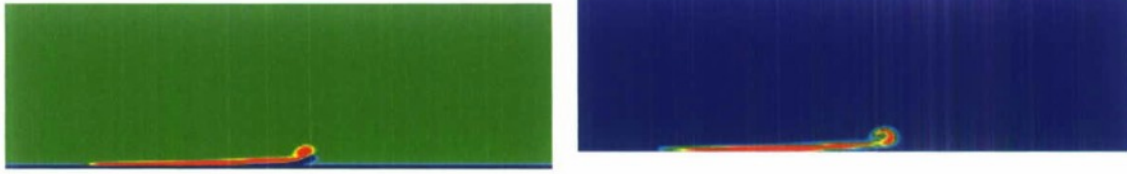
In this series of computations, the source terms are initiated at the time instance $t = 0$ and kept constant for $t > 0$. The unsteady aerodynamic problem is solved with the time step $5 \cdot 10^{-6} \text{ s}$. Consider the case when the SDBD momentum source is directed downstream. The transversal component of vorticity field (scaled from $-3 \cdot 10^{-1} \text{ s}^{-1}$ to $3 \cdot 10^{-1} \text{ s}^{-1}$) and temperature field (scaled from 290 K to 291 K) are shown in Fig. 10 at different time instants. The SDBD

actuator generates a longitudinal near-wall jet. The jet head floats to the upper boundary-layer edge and rolls up to a vortex propagating downstream over the boundary layer.

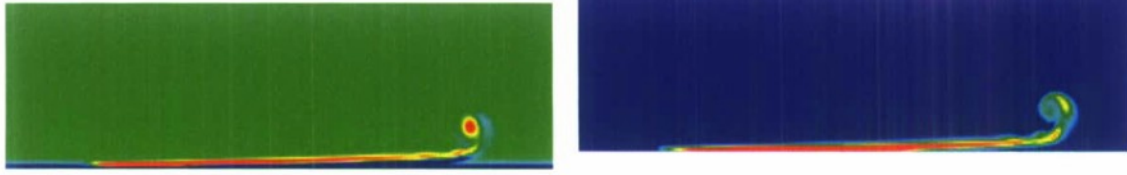
$$t = 3 \cdot 10^{-1} \text{ s}$$



$$t = 7 \cdot 10^{-1} \text{ s}$$



$$t = 15 \cdot 10^{-1} \text{ s}$$



$$t = 25 \cdot 10^{-1} \text{ s}$$

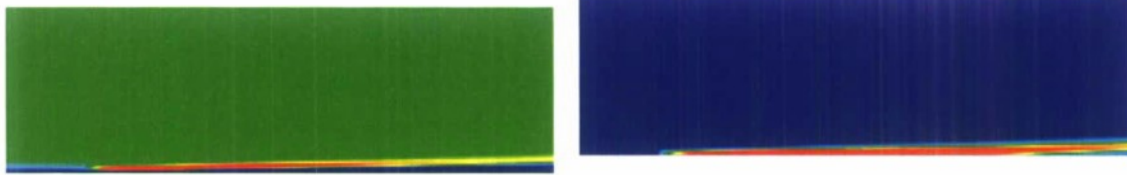


Figure 10 Vorticity and temperature fields at different time instants, steady downstream SDBD forcing.

Another case corresponds to SDBD acting in the upstream direction. Snapshots of the transversal component of vorticity field (scaled from $-3 \cdot 10^{-4} \text{ s}^{-1}$ to $3 \cdot 10^{-4} \text{ s}^{-1}$) and the temperature field (scaled from 290 K to 291 K) are shown in Fig. 11. The SDBD actuator pushes the near-wall fluid upstream and generates a counter-flow jet. This jet interacts with the boundary-layer flow that leads to excitation of strong concentrated vortices propagating downstream. In this case, the SDBD actuator works as a vortex generator.

$$t = 3 \cdot 10^{-1} \text{ s}$$



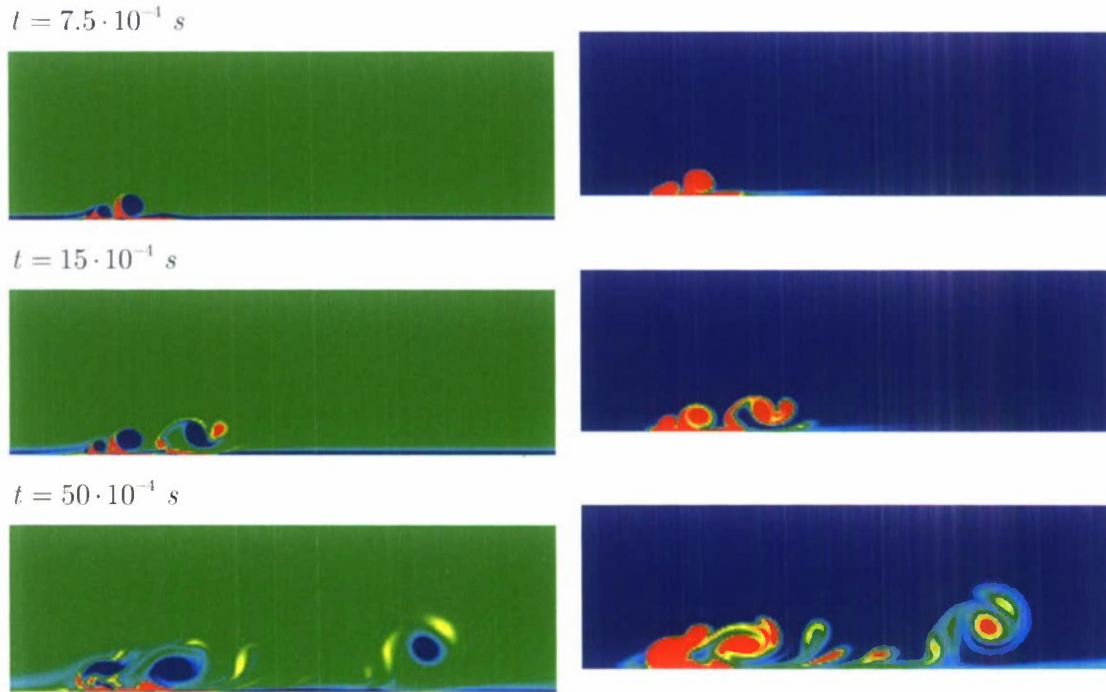


Figure 11 Vorticity and temperature at different time instants, steady upstream SDBD forcing.

2.3.2 Unsteady SDBD forcing

An unsteady SDBD forcing is simulated by repetition of SDBD cycles as schematically shown in Fig. 12. It is assumed that when the discharge is on, the momentum and heat sources are described by the formulae of Section 2.2. When the discharge is off, the sources are zero. The momentum and heat sources are modulated with time as

$$\varphi(t) = \begin{cases} \sin \omega t, \sin \omega t \geq 0 \\ 0, \sin \omega t < 0 \end{cases} \quad (2.40)$$

Here the circular frequency is $\omega = 2\pi U_{\infty} / L_d \approx 10^4 \text{ s}^{-1}$ that corresponds to the modulation period $T = 6 \cdot 10^{-4} \text{ s}$.

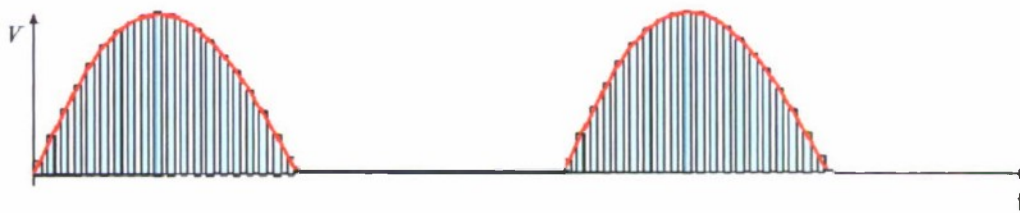


Figure 12 Schematic distribution of SDBD induced source modulation.

Snapshots of the transversal vorticity field (scaled from $-3 \cdot 10^{-4} \text{ s}^{-1}$ to $3 \cdot 10^{-4} \text{ s}^{-1}$) and the temperature field (scaled from 290 K to 291 K) are shown in Fig. 13 for the case of downstream forcing. The SDBD actuator generates a sequence of longitudinal near-wall pulsating jets. In the far field, these jets roll up to vortices propagating downstream over the upper boundary-layer edge.

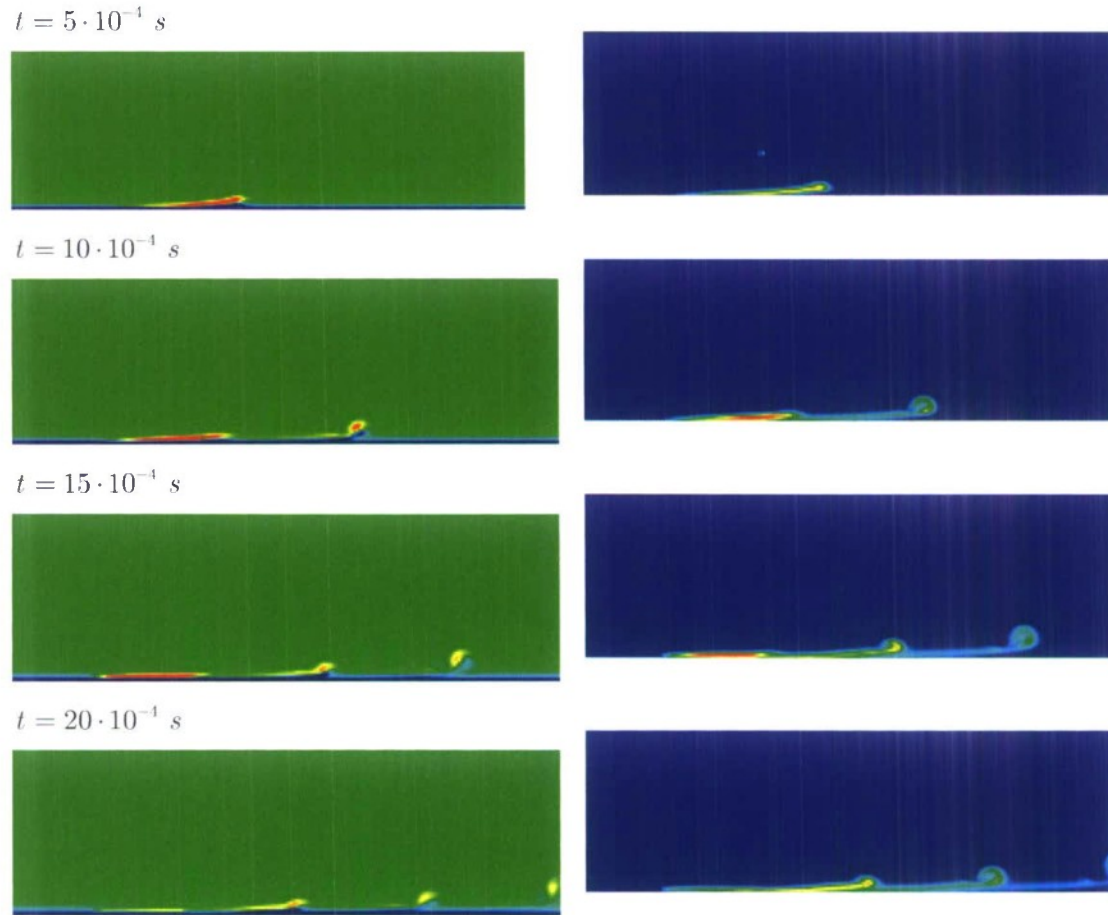


Figure 13 Vorticity and temperature fields at different time instants, unsteady SDBD acts downstream.

The case of upstream SDBD forcing is illustrated by snapshots of the transversal vorticity field (scaled from $-3 \cdot 10^{-4} \text{ s}^{-1}$ to $3 \cdot 10^{-4} \text{ s}^{-1}$) and the temperature field (scaled from 290 K to 291 K), which are shown in Fig. 14. The SDBD actuator generates strong concentrated vortices which propagate over the boundary layer and strongly perturb the near-wall flow.

The foregoing numerical solutions demonstrate that by choosing appropriate distributions of applied voltage it is feasible to achieve quite different aerodynamic effects on the near-wall flow.

This flexibility and very short characteristic timescales make SDBD actuators attractive for control of the near-wall flows associated with the boundary-layer separation, laminar-turbulent transition or a combination of both.

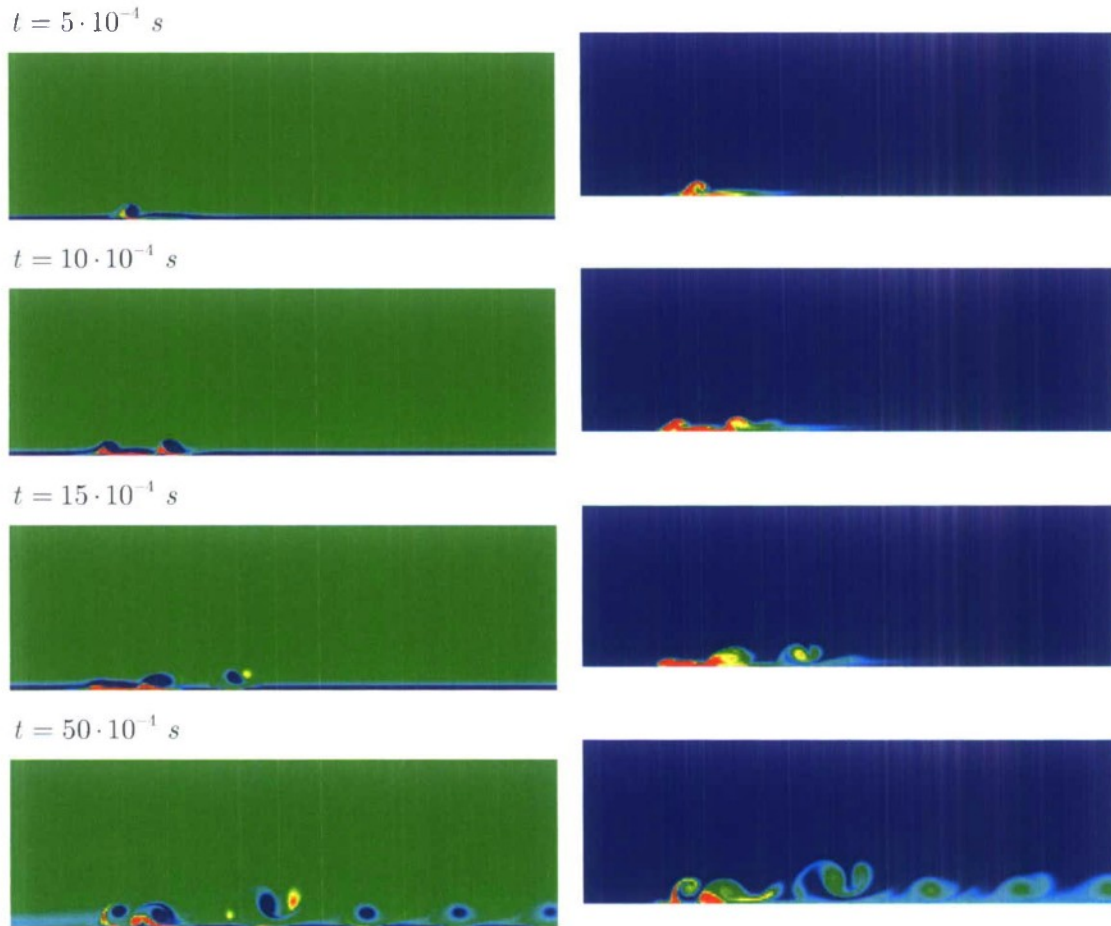


Figure 14 Vorticity and temperature fields at different time instants, unsteady SDBD acts upstream.

2.4 Vortex flow over a supersonic delta wing at angles of attack

Data relevant to vortex structures and their control for delta wings in supersonic flow are very limited. This motivated us to perform numerical simulations of the vortex flow past a delta wing with sharp leading edges at supersonic speeds (freestream Mach number 1.5) and estimate feasibility of the vortex flow control using SDBD actuators.

2.4.1 Problem formulation and numerical method

Consider 3D viscous flow past a delta wing at the free-stream Mach number 1.5 and various angles of attack. The delta wing configuration is shown in Figure 15: the apex angle is 60° , and

the leading-edge sweep angle $\Lambda = 60^\circ$. The wing has zero thickness and sharp leading and trailing edges.

Numerical solutions are obtained using an implicit finite-volume method. Three-dimensional Navier-Stokes equations are approximated by a conservative scheme. The flux vector is evaluated by an upwind, flux-difference splitting of Roe [39]. MUSCL algorithm is applied with the third order TVD space discretization [40]. An Euler implicit discretization in time of the governing equations is combined with a Newton-type linearization of the fluxes to obtain the system of algebraic equations [41]. This system is solved using a point Gauss-Seidel scheme.

The no-slip boundary conditions are imposed on the delta wing surface. Temperature on the wing surface equals to the adiabatic wall temperature. On the outflow boundary, the unknown variables are extrapolated using the linear approximation. On the inflow boundaries, the conditions correspond to free stream. Due to flow symmetry, problem is solved only for one half of the delta wing with symmetry conditions on the plane $y = 0$.

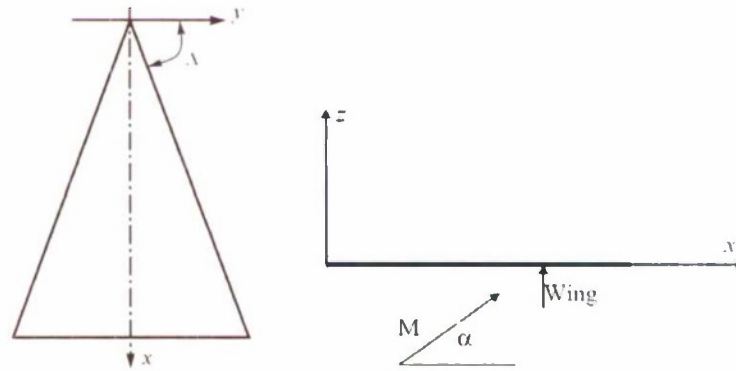


Figure 15 Delta wing configuration and coordinate system.

2.4.2 Cross-flow topology

In order to specify the parameter space for computations, we have analyzed available data on vortex flows past supersonic delta wings. Different cross-flow patterns, which were observed experimentally and numerically over the leeward side of delta wings at various angles of attack [42-44], are summarized in Fig. 16 in terms of Mach number normal to the leading edge $M_N = M_\infty \cos \Lambda \sqrt{1 + \sin^2 \alpha \tan^2 \Lambda}$ and the angle of attack normal to the leading edge $\alpha_N = \tan^{-1}(\tan \alpha / \cos \Lambda)$. With the help of the flow visualization data (vapor-screen photographs, tuft and oil-flow photographs) and surface pressure data, the flow patterns were subdivided into seven types: 1) classical vortex, 2) vortex with shock, 3) separation bubble with no shock, 4) separation bubble with shock, 5) shock with no separation, 6) shock induced separation, 7) no shock and no separation.

More detailed topology suggested in Ref. [44] is shown in Fig. 17. The gray lines (I, II etc.) depict boundaries shown in Fig. 16. The colored lines 1, 2, 3, 4 and 5 show the new details: the green line 1 separates the flow regimes without and with the secondary separation; the yellow line 2 separates the flow regimes with tertiary separation; the region above the blue line 3 corresponds to the flow with a shock wave under the primary vortex; the region below the blue

line 3 corresponds to the flow with no shock under the primary vortex; the brown region 4 corresponds to transition between regimes with and without shock wave above the primary vortex; the red line 5 separates the flow regimes with and without shock between the primary vortices.

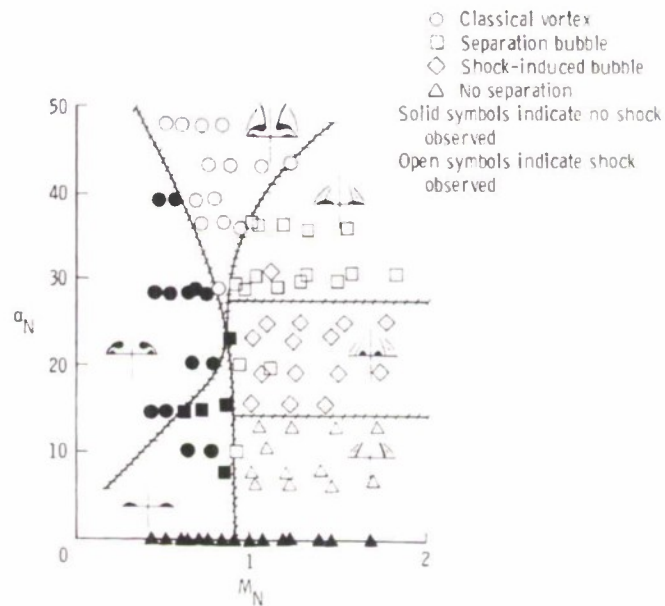


Figure 16 Cross-flow topology reported in Ref. [42].

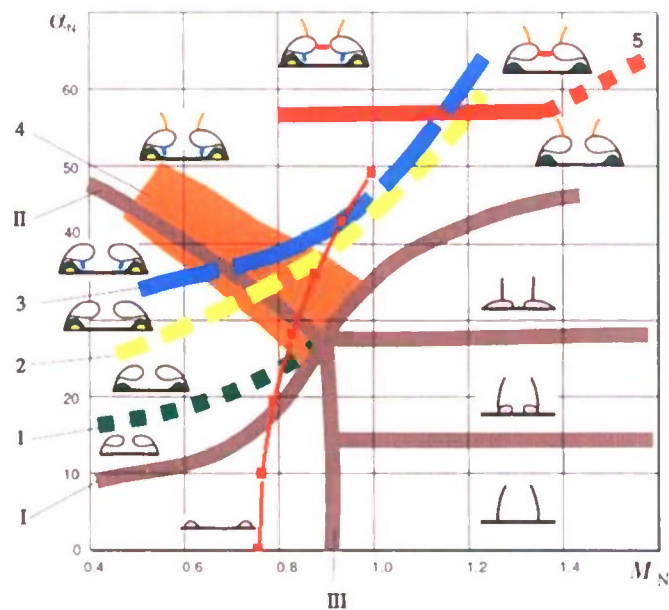


Figure 17 Refined cross-flow topology suggested in Ref. [44], red line with squares – our points.

In all cases, the flow pattern is symmetric because of sharp leading edges of a thin delta wing. Note that the cross-flow diagrams are presented in terms of inviscid parameters α_N and M_N , while flow separations depend on the Reynolds number. Therefore, the flow regimes with secondary and tertiary separation may disagree with these diagrams. The number of separations can increase as the flow approaches the trailing edge [43].

Using the aforementioned data we specify the following set of flow parameters for our computations: the freestream Mach number $M_\infty = 1.5$, the stagnation temperature $T_0^* = 300$ K, the Reynolds number $Re_\infty = \rho_\infty^* U_\infty^* L^* / \mu_\infty^* = 2 \times 10^6$, where $L^* = 1$ m is length of the delta wing; and angles of attack: $\alpha = 0^\circ, 5^\circ, 10^\circ, 15^\circ, 20^\circ, 25^\circ, 30^\circ$. The corresponding points in the $M_N - \alpha_N$ plane are shown in Fig. 17 by the red line with squares.

2.4.2 Vortex flow patterns and aerodynamic forces

Our numerical solutions gave the cross-flow patterns consistent with the diagrams shown in Fig 17. As an example, Figures 18-22 illustrate the case of $\alpha = 30^\circ$ that corresponds to the regime with shocks above and under the primary vortex. These shocks are clearly seen in Fig. 18. The cross-flow streamline patterns (Fig. 19) show that the secondary separation is formed in the wing mid-span under the primary vortex. Substantial differences between the pressure distributions at the stations $x = 0.25$ and $x = 0.5$ (Fig. 20) indicate that the conical pattern breaks down somewhere in between of these stations. This is confirmed by 3D distributions of vorticity (Fig. 21) and streamlines (Fig. 22).

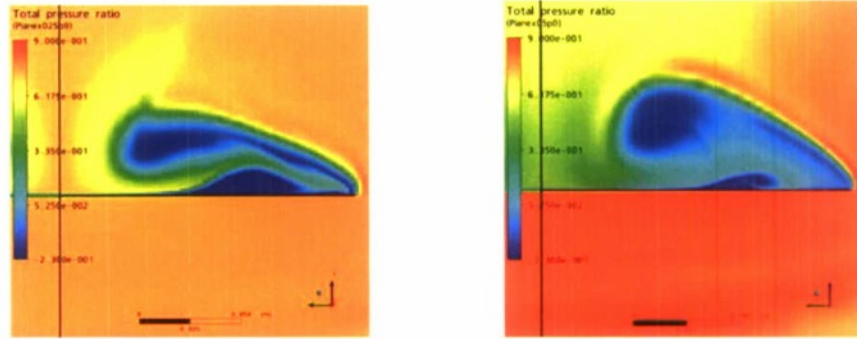


Figure 18 Total pressure ratio field at $x = 0.25$ (left) and $x = 0.5$ (right), $\alpha = 30^\circ$.

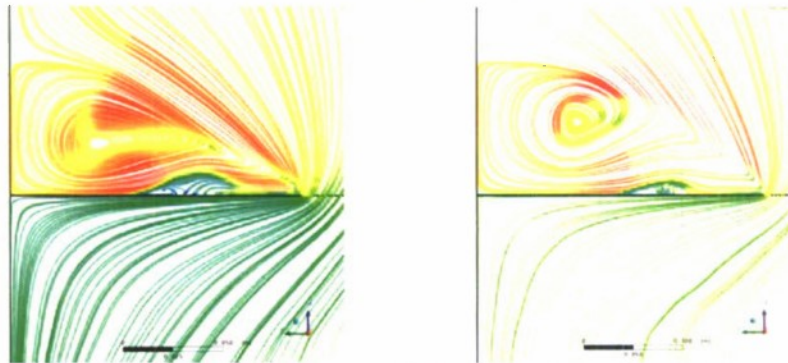


Figure 19 Streamlines in the stations $x = 0.25$ (left) and $x = 0.5$ (right), $\alpha = 30^\circ$.

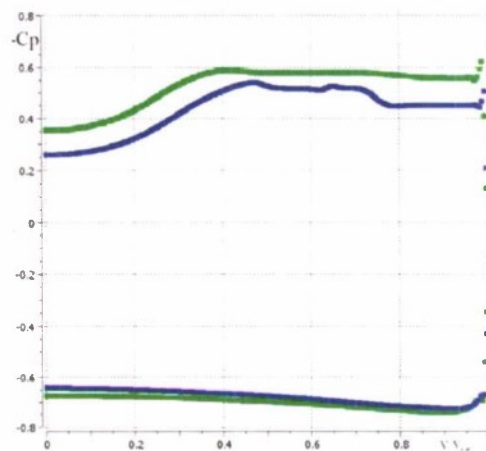


Figure 20 Pressure coefficient for $x = 0.25$ (green line) and $x = 0.5$ (blue line), $\alpha = 30^\circ$.



Figure 21 Isosurface of constant vorticity, $\alpha = 30^\circ$.

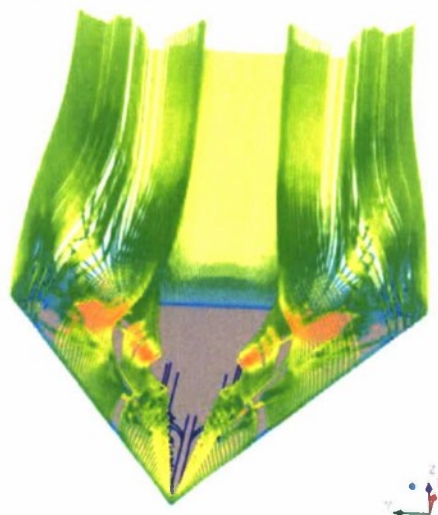


Fig. 22 Streamlines near the delta wing, $\alpha = 30^\circ$.

The integral lift and drag coefficients are shown in Fig. 23 as functions of the angle of attack. The wing aerodynamic performance degrades as the angle of attack exceeds 25° . This correlates with the vortex breakdown that occurs near the wing trailing edge at $\alpha \approx 25^\circ$ and quickly moves upstream as α increases. Detailed analysis of the flow patterns showed that the wing aerodynamic performance depends on the locus of the conical flow breakdown over the wing surface.

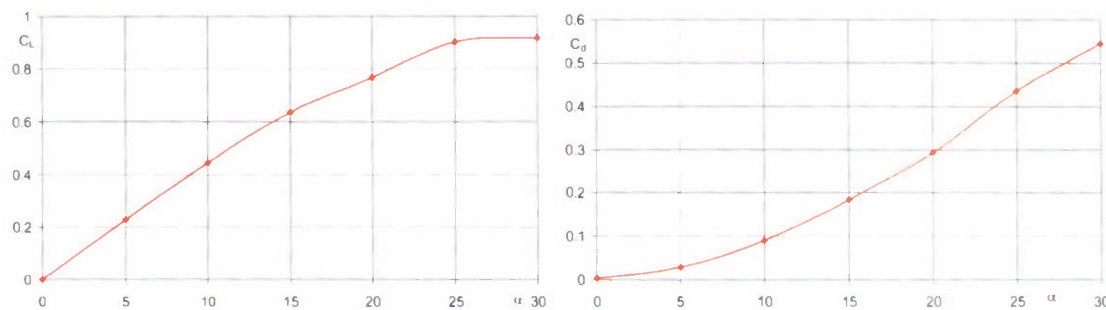


Figure 23 Lift coefficient (left) and drag coefficient (right) versus angle of attack.

2.5 Vortex flow control strategy

As shown in Section 2.4, the delta wing aerodynamic performance depends on the locus where the conical vortex structure breaks down. This suggests that the high-angle-of-attack flow control strategy should be focused on the control of vortex breakdown over the wing leeward side. This phenomenon is associated with a large-scale instability of vortices that is characterized by rapid deceleration and eventual stagnation of the vortex core flow as well as growth of the vortex core cross-section. Much effort has been attempted to understand the physics of this flow phenomenon (see the review articles by Hall [45], Leibovich [46], Escudier [47], Délery [48], Althaus et al. [49], Lucca-Negro and O'Doherty [50]).

The need to control the vortex breakdown over a delta wing at high angles of attack has motivated researchers to propose various flow control techniques [51] including: mechanical devices such as leading-edge flaps [52,53], apex fences [54], canards, strakes, leading-edge-extensions (LEXs), or double-delta wing [55-62] and pneumatic techniques such as trailing-edge blowing [63-68] or suction [69], along-the-core blowing technique [70-73], spanwise blowing [74,75] and some other blowing/suction techniques [76,77] with different blowing/suction locations and orientations.

It is generally believed that the trailing-edge blowing or suction techniques delay vortex breakdown by decreasing the downstream pressure gradient, and along-the-core blowing technique delays vortex breakdown by increasing the axial velocity, i.e., a reduction in the swirl number. Dixon [74] believed that spanwise blowing on the wing provides sweep-like effects as the blowing jets are entrained in the leading-edge vortices. Bradley and Wray [76] credited the success of their blowing technique to the increase in the vortex stability, which to some extent is related to the longitudinal flow in the vortex core. For canards, strakes, leading-edge-extensions, or double-delta wing [55-62], these devices manage vortex breakdown by modifying the flow

field and inducing a nonuniform distribution of local angles of attack at the wing, leading to the generation of a non-conical vortex formation and the corresponding delay in vortex breakdown.

SDBD actuators may be advantageous compared to the aforementioned techniques. This motivated Visbal and Gaitonde [38] to conduct numerical simulation of the DBD actuator effect on the vortical flow above a swept delta wing at high angles of attack in low-speed (Mach=0.1) free stream. With the actuator located near the apex, significant movement of the vortex breakdown location and a dramatic transformation of the shear-layer sub-structures were predicted. Hereafter we discuss results of our numerical simulations of the SDBD effect on the vortex flow past a supersonic delta wing introduced in Section 2.4.

2.6 Vortex flow control using symmetric SDBD forcing

Consider the wing-apex SDBD, leading-edge SDBD and multi-element SDBD actuators schematically shown in Fig. 24. These configurations are symmetric with respect to the wing centerline, and computations have been carried out for one half of the total flow region with the symmetry conditions imposed on the plane $z = 0$.

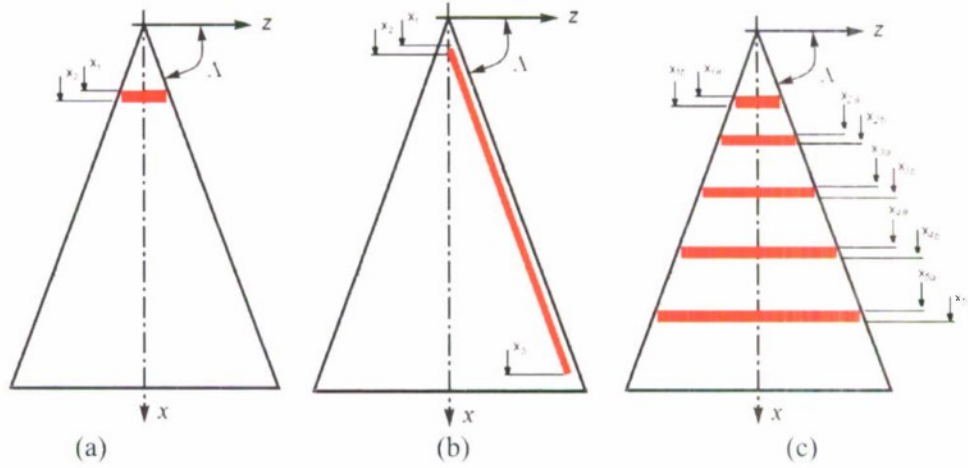


Figure 24 Red lines shows SDBD regions for (a) the wing-apex actuator, (b) the leading-edge actuator and (c) the multi-element actuator.

For the wing-apex and multi-element actuators, the body force components are

$$F_x = F_L, F_L = F_0 f_1(y), f_1(y) = \exp\left(-\frac{(y - y_0)^2}{y_0^2}\right), \quad (2.41)$$

$$F_y = -0.3F_0 f_2(y), f_2(y) = \begin{cases} -y(y - 2y_0)/y_0^2, & 0 \leq y \leq 2y_0 \\ 0, & y > 2y_0 \end{cases}, \quad (2.42)$$

For the leading-edge actuator, the body force F_L is perpendicular to the leading edge. In this case, the streamwise and spanwise components are determined as $F_x = -F_L \cos \Lambda$,

$F_z = F_L \sin \Lambda$. The heat source term in the energy equation is approximated as $Q = Q_0 f_1(y)$. For all cases, $F_0 = 10^4 \text{ N/m}^3$, $y_0 = 3 \times 10^{-5} \text{ m}$, $Q_0 = 2 \times 10^9 \text{ W/m}^3$, the width of SDBD region is 1.5 cm.

2.6.1 Solutions for the wing-apex actuator

Consider the wing-apex actuator (Fig. 24a) with the boundaries of the SDBD forcing region $x_1 = 3 \text{ cm}$ and $x_2 = 4.5 \text{ cm}$. By changing sign of F_L we have simulated SDBD acting downstream ($F_L > 0$) and upstream ($F_L < 0$). In the cases of $\alpha = 0^\circ$ and $\alpha = 5^\circ$, there is no appreciable effect of SDBD on the flow field because there is no global separation from the wing leading edges. For $\alpha = 10^\circ$ (Fig. 25), the SDBD actuator affects the wall temperature field and the streamline pattern. First evidence of the vortex breakdown is observed near the wing trailing edge in the case of no SDBD forcing (a).

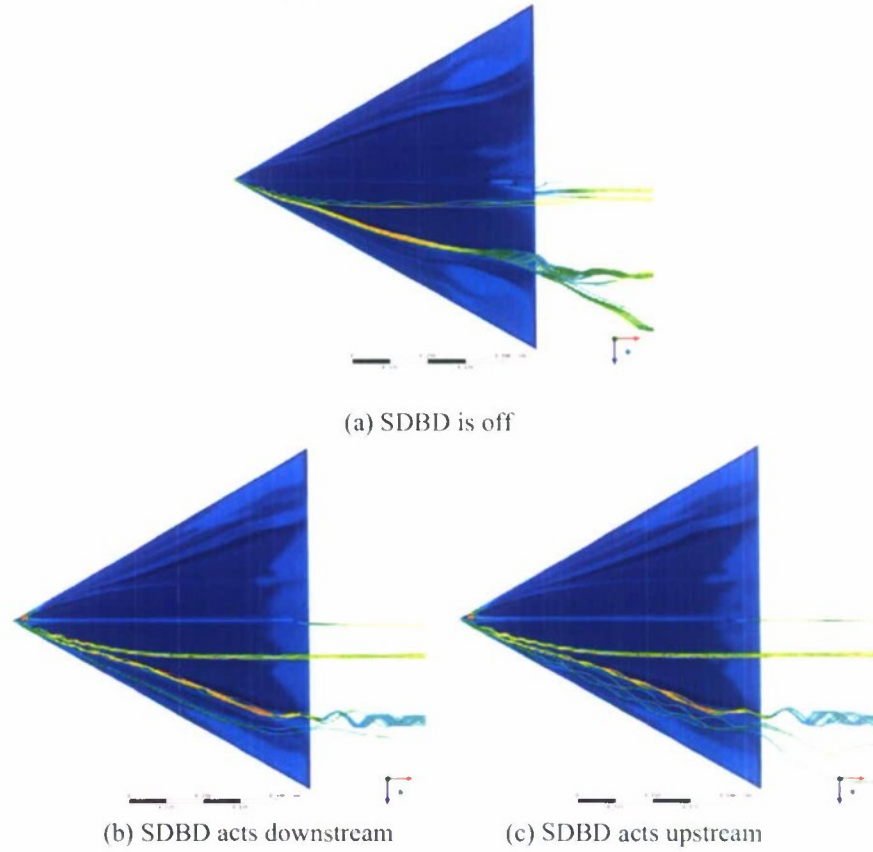


Figure 25 Streamlines and surface temperatures on the leeward side at $\alpha = 10^\circ$.

For $\alpha = 20^\circ$ (SDBD is off) a well-developed vortex is seen in a mid-chord station (Fig. 26a). The burst locus moves downstream with the SDBD acting downstream (Fig. 26b), and it moves upstream with the SDBD acting upstream (Fig. 26c). This example demonstrates that the vortex

breakdown locus can be controlled by the SDBD forcing near the delta-wing apex. This is consistent with the low-speed modeling of Visbal and Gaitonde [38]. However the integral aerodynamic forces (lift and drag coefficients shown in Figs. 27 and 28) are weakly affected. Presumably the aerodynamic loads at supersonic speeds are not so sensitive to the vortex burst locus. For $\alpha \geq 25^\circ$, the influence of DBD on the vortex breakdown is not so clear, because the breakdown point is very close to the wing apex in all three cases.

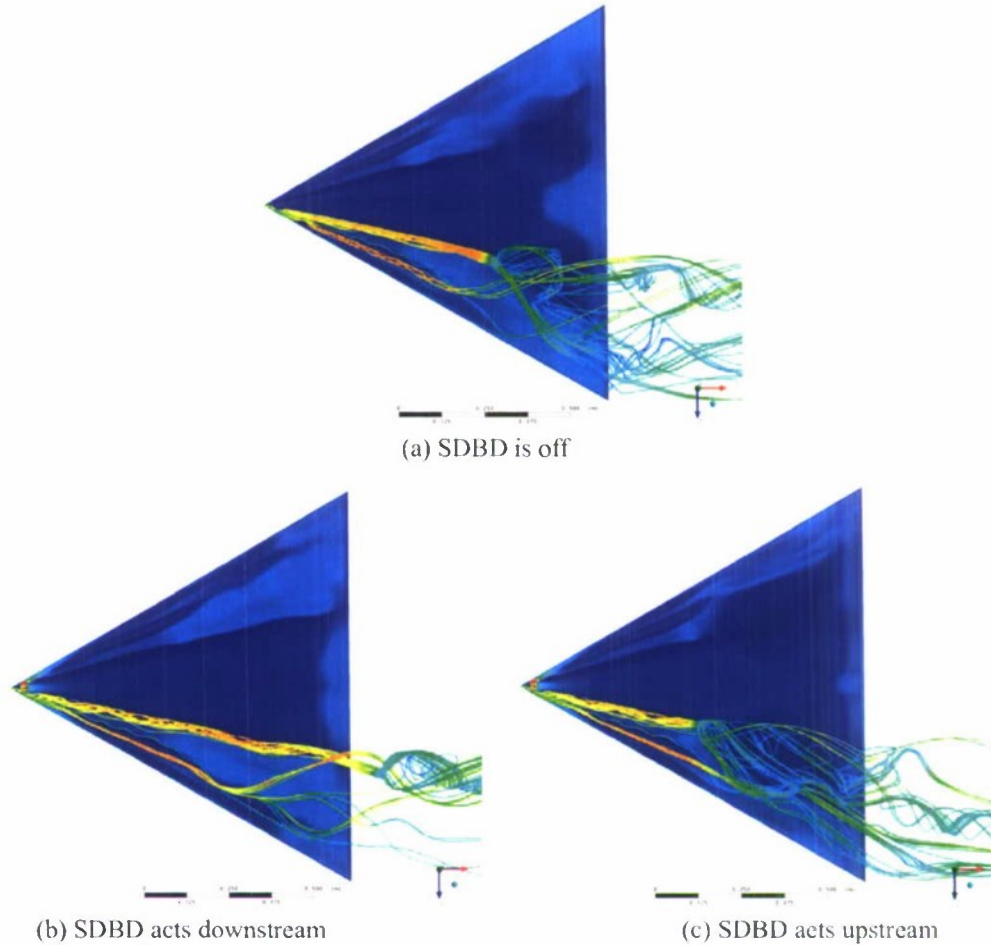


Figure 26 Streamlines and surface temperatures on the leeward side at $\alpha = 20^\circ$.

For sufficiently high angles of attack, the flow field may evolve with time. To clarify this issue we performed direct numerical simulation of unsteady vortex fields for the case of $\alpha = 20^\circ$. As expected the primary-vortex breakdown slowly moves along the wing surface. The secondary vortex reveals more unsteady oscillatory behavior. This unsteadiness is observed both with and without SDBD forcing. Nevertheless, appreciable migrations of the burst locus weakly affect the lift coefficient C_L (it varies in the range $0.836 < C_L < 0.840$).

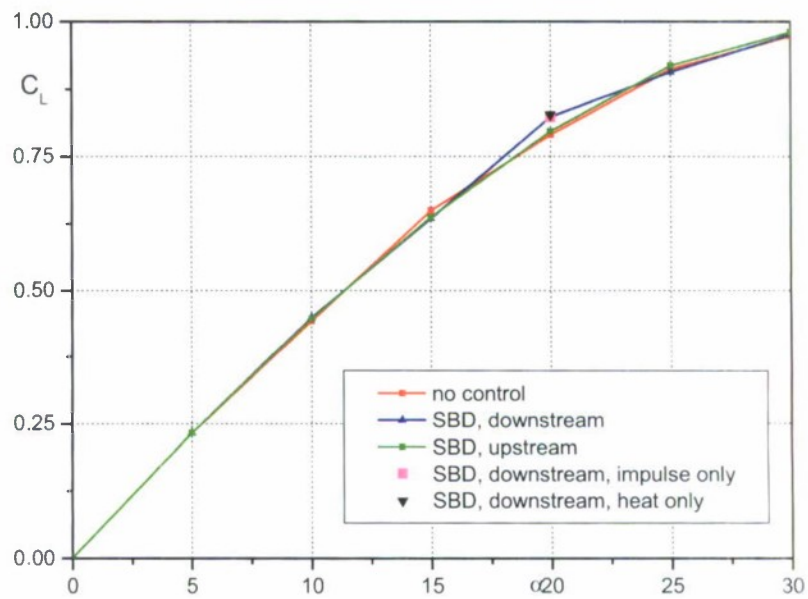


Figure 27 Lift coefficient versus angle of attack.

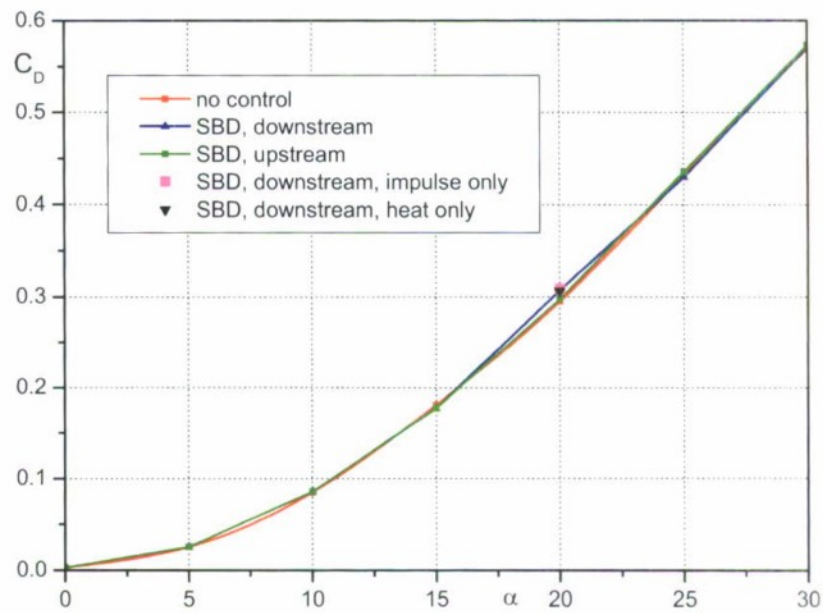


Figure 28 Drag coefficient versus angle of attack.

2.6.2 Solutions for the leading-edge actuator

Consider the leading-edge SBD actuator shown in Fig. 24b. The boundaries of SBD forcing are specified as $x_1 = 3$ cm, $x_2 = 6$ cm and $x_3 = 90$ cm. Figure 29 shows the drag polar, data for the wing-apex actuator are also presented for comparison. In this figure: the red line corresponds to the case of SBD off; the blue line corresponds to the case when wing-apex SBD induces the momentum source in the positive x -direction (downstream forcing); the green line corresponds to the case when the wing-apex SBD induces the momentum source in the negative x -direction (upstream forcing); the magenta square corresponds to the case when the leading-edge SBD induces the momentum perpendicular to the leading edge at $\alpha = 20^\circ$. Additional computations were carried out to distinguish the SBD momentum effect from the SBD heating effect. The black triangle corresponds to the case when the momentum source is included into Navier-Stokes equations while the heat source is not. The cyan triangle corresponds to the opposite situation – the heat source is on while the momentum source is off. In all the cases, SBD forcing produces small effect on the wing aerodynamic performance.

Figure 30 illustrates the influence of SBD on 3D streamlines and the wall temperature at the angle of attack $\alpha = 20^\circ$. When SBD is off (Fig. 26a), the vortex burst is observed in the mid-chord station. The momentum source (Fig. 30a) and the heat source (Fig. 30b) lead to an appreciable downstream shift of the vortex burst locus. Nevertheless, they weakly affect the integral aerodynamic forces shown in Fig. 29.

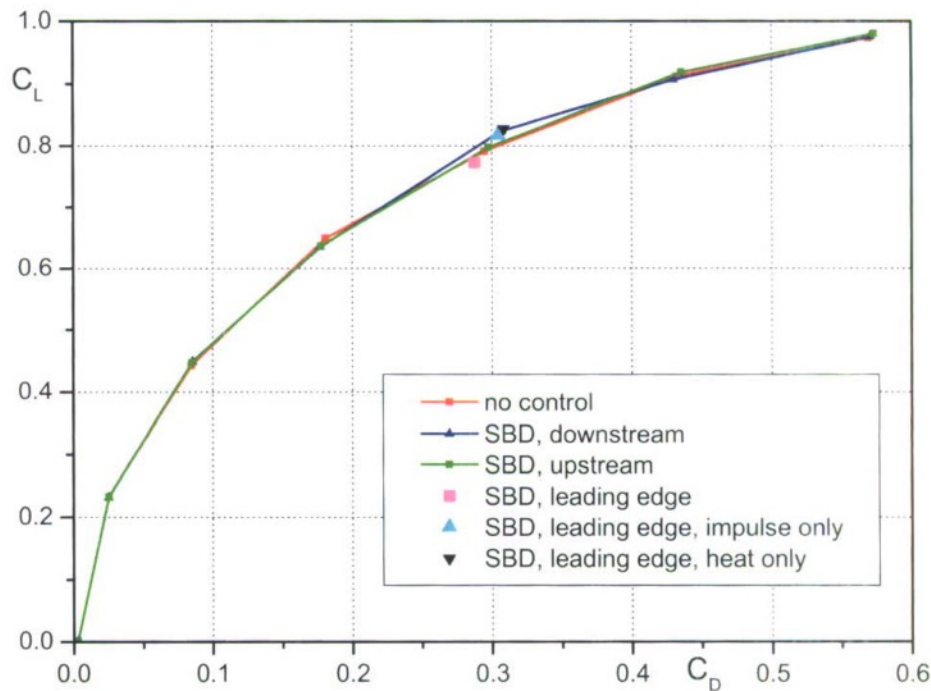


Figure 29 Drag polar.

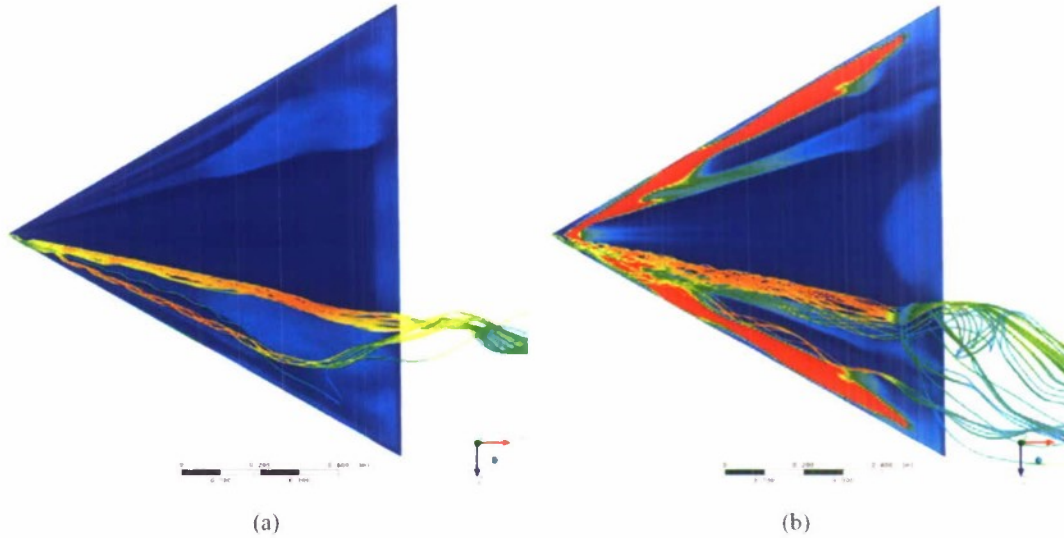


Figure 30 The leading-edge SDBD effect on the vortex flow field at $\alpha = 20^\circ$; (a) the momentum source is on while the heat source is off; (b) the heat source is on while the momentum source is off.

2.6.3 Solutions for the multi-element actuator

Consider the multi-element configuration comprising five SDBD regions (Fig. 24c). This configuration resembles the SDBD actuator used for the low-speed wind tunnel experiments in ITAM [78]. The coordinates of the SDBD-forcing boundaries, x_{in} and x_{ib} , are given in Table 2.

Figure 31 shows the five-element SDBD effect on the flow streamlines and the wall temperature pattern. Similar to the configurations considered in previous sections, this actuator causes appreciable downstream shift of the vortex burst. Nevertheless, the integral aerodynamic coefficients vary in the range of 3% only.

Table 2

Number of SDBD strip	x_{in}, m	x_{ib}, m
1	0.03	0.045
2	0.15	0.165
3	0.4	0.415
4	0.6	0.615
5	0.8	0.815

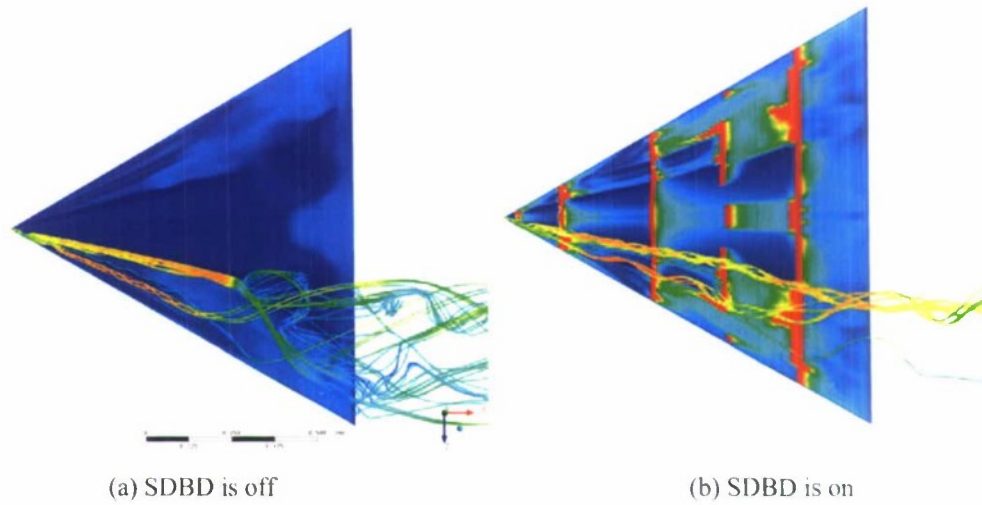


Figure 31 The five-element SDBD effect on streamlines and surface temperature, $\alpha = 20^\circ$.

2.7 Vortex flow control using asymmetric SDBD forcing

Herein we discuss numerical simulations of aerodynamic moments induced by asymmetric SDBD forcing on the aforementioned delta wing. The problem is formulated for the total delta wing configuration without applying the symmetry conditions on the symmetry plane. This allows us to investigate feasibility of the rolling moment control by asymmetric SDBD forcing.

The computational grid is obtained by doubling of the grid used for the symmetrical problem. It has approximately 9×10^6 nodes. In the boundary-layer and leading-edge regions, the grid nodes are clustered to resolve fine flow structures.

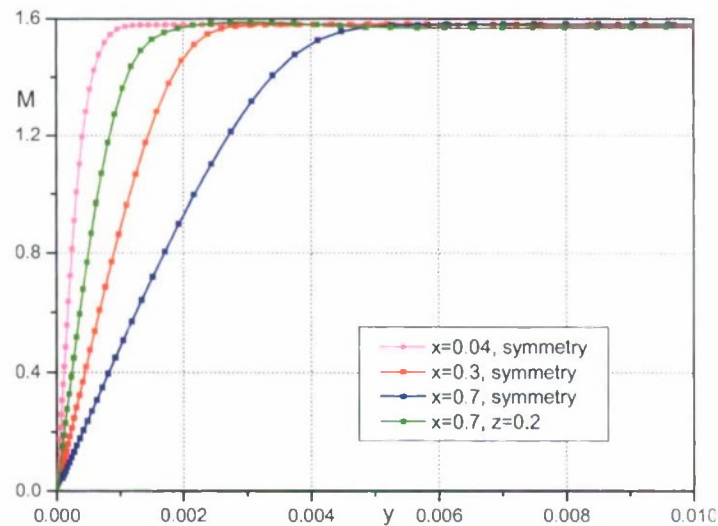


Figure 32 Boundary layer profiles.

First series of computations was conducted for the case of $\alpha = 5^\circ$. Figure 32 shows the boundary layer profiles (the local Mach number versus the normal coordinate y) on the symmetry plane at $x = 0.04$ (magenta line), $x = 0.3$ (red line) and $x = 0.7$ (blue line). The boundary layer profile at the point $(x, z) = (0.7, 0.2)$ is shown by the green line. In all cases, there are more than 25 grid nodes in the boundary layer that provides sufficient accuracy for simulations of the near-wall flow structures.

In order to validate the code and grid refinements, we simulated the case of $\alpha = 20^\circ$ without SDBD forcing and compared the numerical solution with that obtained with the flow symmetry conditions. As shown in Fig. 33, the agreement in terms of the lift coefficient is good.

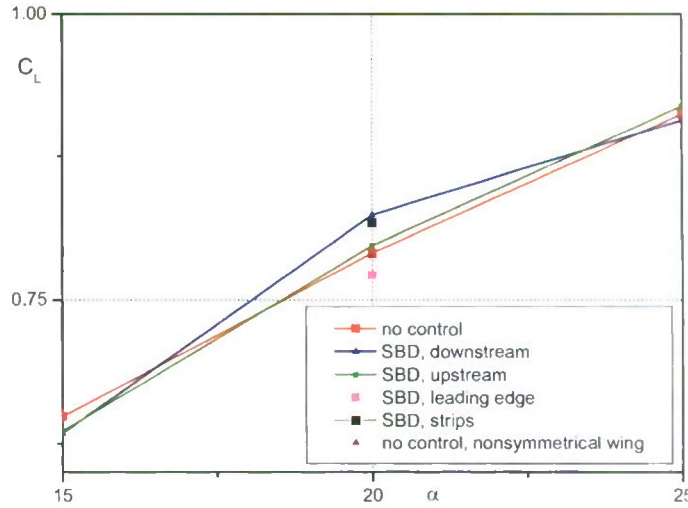


Figure 33 $C_L(\alpha)$ without SDBD forcing calculated using the flow symmetry conditions (red line) and for the total wing (purple triangle).

2.7.1 Solutions for the wing-apex actuator

Numerical simulations of the asymmetric SDBD forcing were conducted for the configuration shown in Fig. 34, where the forcing region is indicated by the red strip. The SDBD induced source terms for the x - and y -momentum equations are approximated by the analytical relations, which are similar to those given in Section 2.2.

$$\begin{aligned} F_x(x, y, t) &= \varphi(t) A_{xF} g_F(x) f(y) \\ F_y(x, y, t) &= \varphi(t) A_{yF} g_F(x) f(y) \end{aligned} \quad (2.43)$$

Here $\varphi(t)$ is a step-function: $\varphi(t) = 0$ for $t \leq 0$, $\varphi(t) = 1$ for $t > 0$. The longitudinal distribution is

$$g_F(x) = \left[1 - \left(\frac{x - x_1}{L_d} \right)^2 \right]^{0.2}, \quad x_1 \leq x \leq x_2, \quad (2.44)$$

$x_1 = 2.5$ cm, $x_2 = x_1 + L_d$, where $L_d = 5$ mm. The distribution normal to the wing surface is

$$f(y) = a_f y \exp \left[-\frac{\sigma_f (y - y_{0F})^2}{2} \right], a_f = 7547 \text{ m}^{-1}, \sigma_f = 10^8 \text{ m}^{-2}, y_{0F} = 0.1, \quad (2.45)$$

where the vertical size is approximately 0.4 mm, $A_{xF} = 10^5 \text{ N/m}^3$ and $A_{yF} = -2 \cdot 10^4 \text{ N/m}^3$.

The heat source is approximated as

$$Q(x, y, t) = \varphi(t) A_{qr} g(x) f(y), \quad (2.46)$$

where $A_{qr} = 10^7 \text{ W/m}^3$.

Figure 35 shows 3D streamlines for symmetrical flow without SDBD forcing (a) and with the downstream forcing (b) for the angle of attack $\alpha = 20^\circ$. In this example, the heat source is zero. The streamlines are released from a small region near the wing apex.

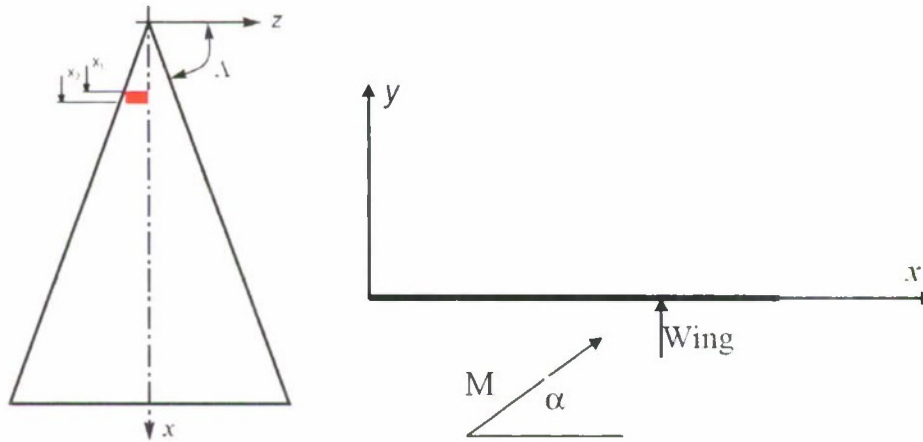


Figure 34 Delta wing scheme and coordinate system, SDBD region is shown by the red strip.

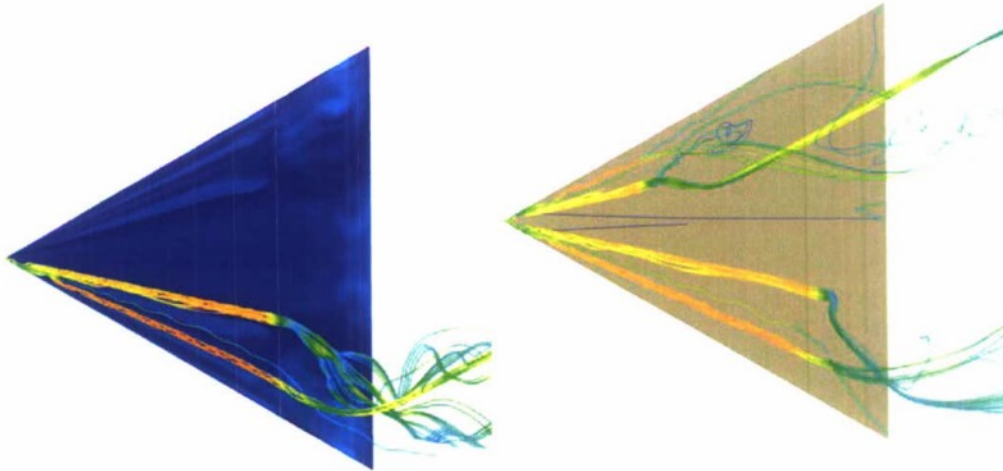


Figure 35 Streamlines and surface temperature at $\alpha = 20^\circ$. (a) – SDBD is off. (b) – SDBD acts downstream on the bottom half plane, the heat source is zero.

It is seen that the vortex burst on the actuated wing surface is slightly delayed. On the non-actuated surface, the burst is shifted upstream significantly. This indicates that the SDBD effect is not local, and the wing-apex actuator affects the global flow pattern in a nontrivial manner.

Figure 36 illustrates the case when the SDBD actuator produces both the downstream momentum source and the heat source. It turned out that solutions were highly unsteady; i.e., the heat source leads to significant increasing of the burst locus oscillations.

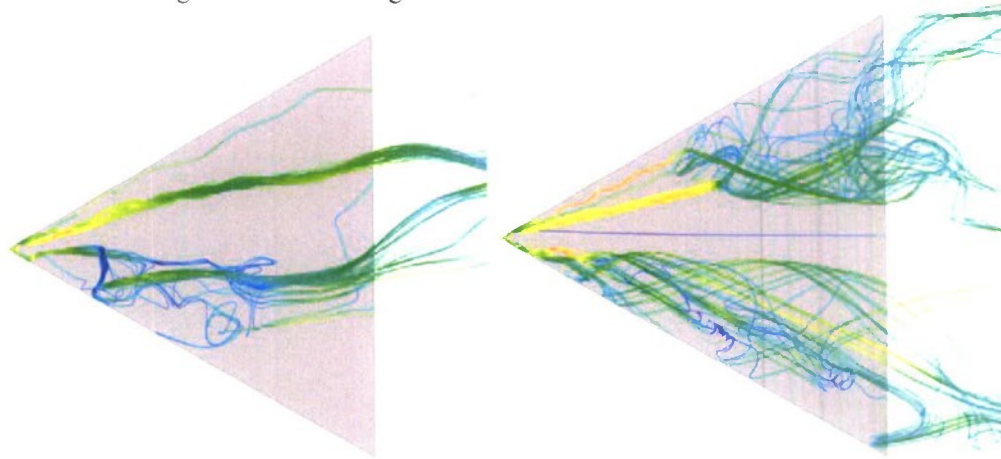


Figure 36 Snapshots of 3D streamline pattern on the leeward wing surface. The SDBD actuator produces both the downstream momentum source and the heat source on the bottom half plane.

2.7.2 Solutions for the leading-edge actuator

Consider the case when the SDBD region is located near the wing leading edge as shown in Fig. 37. The actuator can bow out the wing symmetry plane or toward the wing symmetry plane as shown by the blue arrows.

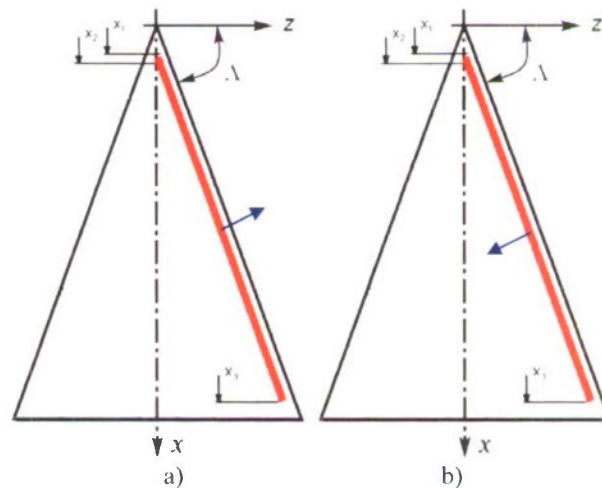


Figure 37 The leading-edge SDBD actuator blows out the wing symmetry plane (a) and toward the wing symmetry plane (b).

Figure 38 shows 3D streamlines over the leeward wing surface for the case shown in Fig. 37a (the actuator blows away from the wing). The left and right plots correspond to different time instants. The SDBD region is schematically shown by the red dashed line. Sudden breakdowns of the streamline patterns indicate bursts of the primary vortices.

Figure 39 illustrates the case when SDBD blows toward the wing symmetry plane (Fig. 37b). A qualitative behavior of the vortex flow is similar to the previous case. The flow is highly unsteady. The vortex bursts move back and forth with appreciable amplitude. This leads to significant oscillations of the rolling moment.

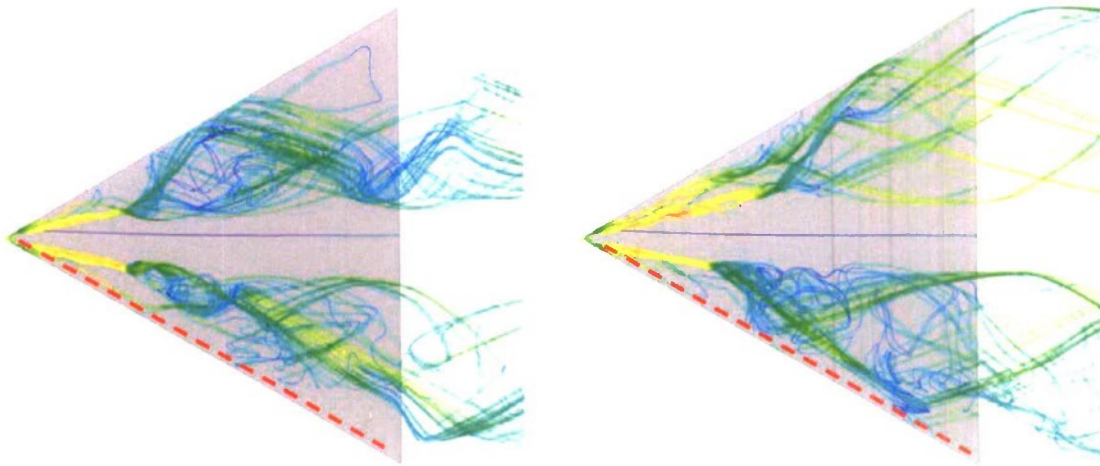


Figure 38 3D streamlines over the leeward wing surface at different time instants. SDBD blows away from the wing (Fig. 37a), the actuator is schematically shown by the red dashed line.

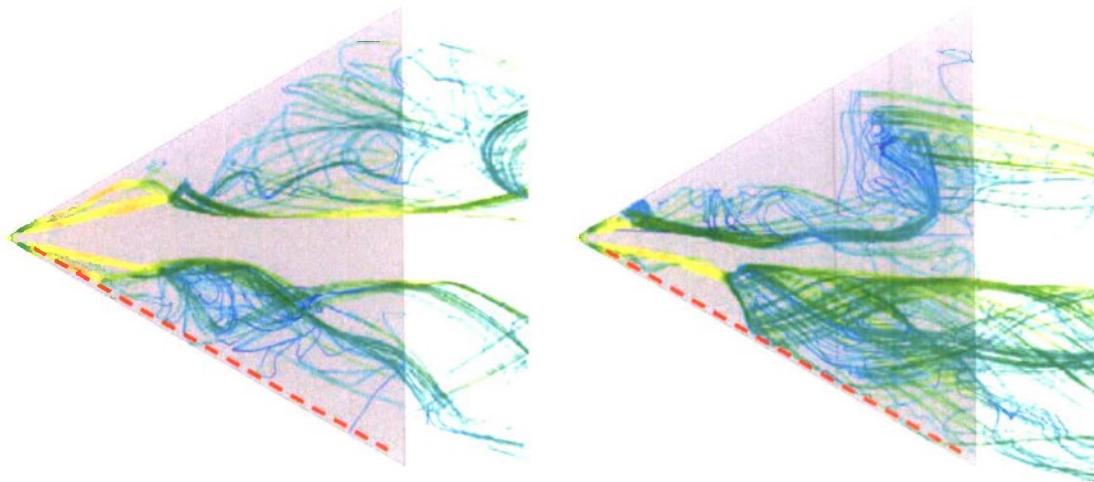


Figure 39 3D streamlines over the leeward wing surface at different time instants. SDBD blows toward the wing (Fig. 37b), the actuator is schematically shown by the red dashed line.

2.7.3 Solutions for multi-element actuator

Consider a multi-element SDBD schematically shown in Fig. 40. The red strips indicate the SDBD elements. The forcing is produced on one side of the wing leeward surface, where $z > 0$. The coordinates x_{ia}, x_{ib} are given in Table 3. The SDBD forcing is directed downstream.

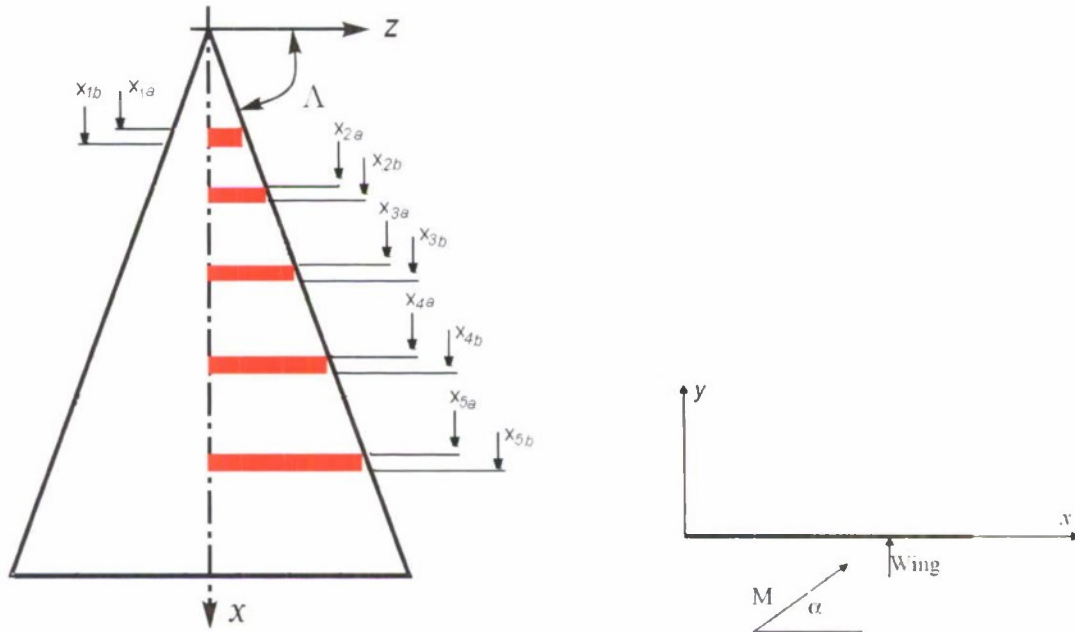


Figure 40 The multi-element actuator on the delta wing. The SDBD elements are shown by red lines.

Table 3 Coordinates of SDBD elements

$i = \text{number of DBD strip}$	x_{ia}, m	x_{ib}, m
1	0.03	0.045
2	0.15	0.165
3	0.4	0.415
4	0.6	0.615
5	0.8	0.815

Figure 41 shows 3D streamline patterns over the leeward wing surface. The actuator is located on the low half plane. It is clearly seen that the SDBD forcing leads to appreciable delay of the vortex bust. Note that the vortex flow is highly unsteady similar to the cases considered in Sections 2.7.1 and 2.7.2. The streamlines and the vortex bust loci oscillate that causes significant pulsations of the aerodynamic coefficients.

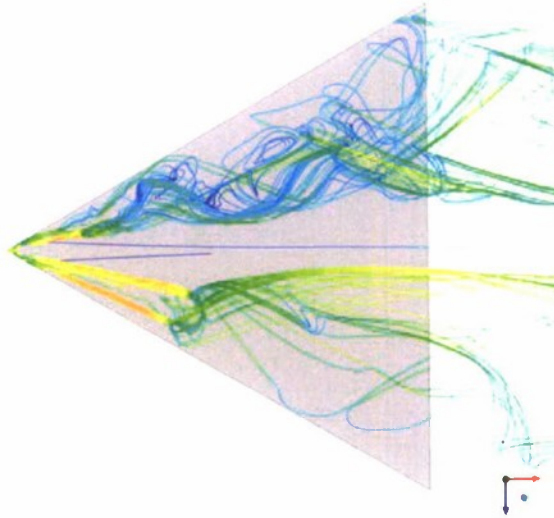


Figure 41 Streamline pattern over the leeward wing surface, the SDBD elements are located on the lower side ($z>0$) and blow downstream.

3. Summary and Impact of Effort

This project includes the two major components: modeling of the surface dielectric barrier discharge (SDBD) and CFD studies of SDBD flow control capabilities.

The first component has been focused on developments of self-consistent theoretical models and robust computational tools providing adequate from-first-principles simulations of heat and momentum sources induced by surface discharges. The physical model and numerical code were developed to predict SDBD process in atmospheric air. The model accounts for air photoionization by UV radiation from discharge zone, approximation of non-local ionization source and universal boundary conditions on the electrode and dielectric surfaces. This allows us to simulate the total SDBD cycle including the discharge formation phase and the discharge relaxation phase.

The numerical solutions showed that the discharge formation phase lasts few tens of nanoseconds and creates plasma. The discharge evolves as a streamer for positive electrode polarity and as a diffusive discharge for negative electrode polarity. The predicted values of the discharge length and the surface charge density agree well with the available experimental data both for positive and negative electrode polarity. This validates the developed physical model and computational code.

Although the discharge formation phase gives negligible contribution to the momentum and heat sources relevant to flow control applications, it provides initial conditions for the relaxation phase. The latter begins when plasma is redistributed in such a way that it shields the external electric field and reduces the air ionization rate in the discharge region to very small value. The ion-electron and ion-ion recombination along with the ion drift motion are main processes in the relaxation phase, which lasts few microseconds. This phase effectively contributes to the momentum and heat sources required for flow control. The momentum-source distributions have

a complicated structure in space. For negative electrode polarity, the body force is an order of magnitude greater than in the case of positive applied voltage.

Using these findings and available experimental data we have developed a physics-based phenomenological model, which sheds light on processes governing the ignition and ceasing of microdischarges for the negative going half-cycle of applied alternating voltage. This model clarifies mechanisms leading to the body force saturation observed in experiments. The obtained analytical formulae capture dependencies of the body force and discharge length on the SDBD parameters. The model has been validated against the experimental data for SDBD actuators having dielectric layers of different materials and thicknesses. The phenomenological model led us to the assumption that the SDBD performance can be improved dramatically by increasing of the volumetric charge of negative ions. This can be done with the help of 'conducting' dielectrics.

Using the body-force values predicted by the phenomenological model and numerical results for the spatial distributions of momentum and heat sources, we have obtained analytical approximations of the SDBD-induced body force and heat source. The source terms were incorporated into Navier-Stokes solver. This computational tool has been used in the second component of the project dealing with SDBD applications to flow control.

To clarify aerodynamic effects produced by SDBD actuator, we have considered a relatively simple flow – the laminar boundary layer on a flat plate in a free stream of low subsonic speed. Numerical solutions of 2D unsteady Navier-Stokes equations showed that the SDBD effect on the near-wall flow strongly depends on time-modulations of the applied voltage. If the discharge produces downstream momentum, then the actuator generates tangential near-wall jets. If the SDBD forcing is directed upstream, the actuator generates strong concentrated vortices. This flexibility and very short characteristic timescales make SDBD actuators attractive for control of the near-wall flows associated with the boundary-layer separation, laminar-turbulent transition or a combination of both.

CFD studies of the vortex flow past a delta wing at high angles of attack have been carried out to estimate feasibility of the vortex flow control using SDBD. Computations were performed for a delta wing with sharp leading edges of 60° sweep angle at the free-stream Mach number $M_\infty = 1.5$, Reynolds number $Re_\infty = 2 \times 10^6$ and angles of attack $0^\circ \leq \alpha \leq 30^\circ$.

First series of computations was conducted without SDBD forcing. It was shown that our numerical solutions are consistent with available experimental and numerical results. Analysis of flow patterns at various angles of attack indicated that the wing aerodynamic performance depends on the locus where the conical vortex structure breaks down. This suggested that the high-angle-of-attack flow control strategy should be focused on control of the vortex breakdown (or vortex burst) over the wing leeside.

In the second series of computations, we have treated the wing-apex SDBD, leading-edge SDBD and multi-element SDBD actuators located on the wing leeside surface. The heat and momentum sources produced by these actuators were symmetric with respect to the wing centerline. It was found that the vortex-burst locus can be controlled by the aforementioned actuators. Namely, the breakdown point moves downstream with the SDBD acting in the downstream direction while it moves upstream with the SDBD acting upstream. However, the integral aerodynamic forces are weakly affected. The actuator causes about 3% variations of the lift and drag coefficients. Presumably the aerodynamic loads are weakly sensitive to the vortex burst locus for the delta

wing and free-stream parameters considered herein. Direct numerical simulations of unsteady flow fields showed that the vortex breakdown evolves with time. Its unsteady behavior is sensitive to the SDBD forcing. Nevertheless, appreciable migrations of the burst locus produce small (less than 2%) effect on the lift coefficient.

In the third series of computations, we considered the same SDBD actuators, which were located on one side of the wing surface. It was expected that an asymmetric SDBD forcing could generate appreciable rolling moment. However, numerical solutions of 3D Navier-Stokes equations indicated that the asymmetric forcing triggers strong oscillations of the vortex burst loci. This, in turn, causes pulsations of the rolling moment. Because of this detrimental effect it is not clear if SDBD actuators are robust for the vortex flow control on supersonic delta wings at high angles of attack. Further numerical and experimental studies are needed to clarify this issue.

References

1. Malmuth, N.D., "Mathematical Fluid Dynamic Modeling of Plasma Stall-Spin Departure Control," Proposal in response to BAA 2001-2, SC 63158-dT, Rockwell Scientific Company., 2001.
2. Shalaev, V., Fedorov, A., Malmuth, N., Zharov, V., and Shalaev, I., "Plasma Control of Forebody Nose Vortex Symmetry Breaking," AIAA Paper No. 2003-0034.
3. Shalaev, V., Fedorov, A., Malmuth, N., and Shalaev, I., "Mechanism of Forebody Nose Vortex Symmetry Breaking Relevant Plasma Flow Control," AIAA Paper No. 2004-842, 2004, Reno NV.
4. Maslov A., *et al* "Plasma Control of Separated Flow Asymmetry on a Cone at High Angle of Attack," AIAA Paper No. 2004-843, 2004.
5. Maslov A.A., Zanin, B.Yu., Sidorenko, A.A., Postnikov, B.V., Fomichev, V.P., and Malmuth, N., "Two-Channel Spark Discharge for Flow Control on a Body of Revolution," AIAA Paper No. 2005-040, 10-13 January 2005, Reno NV.
6. Zhakharov, S.B., Fedorov, A.V., and Malmuth, N.D., "Modeling of Forebody Nose Symmetry Breaking Using Conical Navier-Stokes Solutions," AIAA Paper No. 2006-1257, 9-12 Jan. 2006, Reno NV.
7. Malmuth, N.D., Zhakharov, S.B., and Fedorov, A.V., "Conical Navier-Stokes Modeling of Forebody Vortex Symmetry Plasma Control," AIAA Paper No. 2007-0219, Jan. 2007, Reno NV.
8. Rom, J, *High angle of Attack Aerodynamics, Subsonic, Transonic, and Supersonic Flows*. Springer-Verlag, 1992.
9. Lee, M., Ho, C.M., "Lift Forces of Delta Wings," *Applied Mechanics Reviews* (ASME Book No. AMR077), Vol. 43, No. 9, September, 1990.
10. Visbal, V.M., "Multidisciplinary Computational Aerodynamics," AFOSR Meeting, Long Beach California, Aug. 29-Sept. 2, 2005.
11. Ho, C.M., and Huang, L.S., "Subharmonics and Vortex Merging in Mixing Layers," *Journal of Fluid Mechanics*, Vol. 119, 1982, pp. 443-473.
12. Corke, T.C., and Post, M.L., "Overview of Plasma Flow Control: Concepts, Optimization, and Applications," AIAA Paper No. 2005-563, 10-13 January 2005, Reno NV.

13. Post, M., and Corke, T., "Separation Control on High Angle of Attack Airfoil Using Plasma Actuators," AIAA Paper No. 2003-1024, 2003.
14. Post, M., and Corke, T., "Separation Control Using Plasma Actuators - Stationary and Oscillating Airfoils," AIAA Paper No. 2004-0841, 2004.
15. Malmuth, N., Maslov, A.A., Kozlov, V.V., Zanin, B.Yu., Sidorenko, A.A., Postnikov, B.V., Zverkov, I.D., Starikovskii, A.Yu., "Plasma Control of Separated Flows on Airfoil at High Angle of Attack," Technical Report of Rockwell Scientific Company, ITAM and MIPT, December 2005.
16. Gibalov V.I., and Pietsch G.J., *J. Phys. D: Appl. Phys.*, Vol. 33, 2000, pp. 2618-2636.
17. Roy, S., and Gaitonde, D.V., "Multidimensional Collisional Dielectric Barrier Discharge for Flow Separation Control at Atmospheric Pressures", AIAA Paper 2005-4631, 8-9 June 2005, Toronto, Ontario, Canada.
18. Likhanskii A.V., Shneider M.N., Macheret S.O., Miles R.B., "Modeling of Interaction Between Weakly Ionized Near-Surface Plasmas and Gas Flow", AIAA Paper 2006-1204, Jan. 2006, Reno NV.
19. Soloviev V.R., Krivtsov V.M., Konchakov A.M., Malmuth N.D, 2008, "Surface Barrier Discharge Simulation in Air for Constant Applied Voltage", AIAA Paper No. 2008-1378, Jan. 2008, Reno NV.
20. Soloviev V.R., Konchakov A.M., Krivtsov V.M, Aleksandrov N.L., "Numerical Simulation of a Surface Barrier Discharge in Air", *Plasma Physics Reports*, Vol. 34, 2008, pp. 594-608.
21. Aleksandrov N.L., Bazelian A.E., Bazelian E.M., Kochetov I.V., "Long Streamer Modeling in Atmospheric Pressure Gas", *Plasma Physics Rep.*, Vol. 21, 1995, pp. 60-80.
22. Aleksandrov N.L., Visikailo F.I., Islamov R.Sh., Kochetov I.V., Napartovich A.P., Pevgov V.G., "Electron Distribution Function in Mixture $N_2:O_2=4:1$ ", *High Temp.*, Vol. 19, 1981, pp. 22-27.
23. Georgiou G.E., Papadakis A.P., Morrow R., Metaxas A.C., "Numerical Modeling of Atmospheric Pressure Gas Discharges Leading to Plasma Production", *J. Phys. D: Appl. Phys.*, Vol. 38, 2005, pp. R303-R328.
24. Kossyi I.A., Kostinsky A.Yu., Matveyev A.A., Silakov V.P., "Kinetic Scheme of the Non-Equilibrium Discharge in Nitrogen-Oxygen Mixtures", *Plasma Sources Sci. Technol.*, 1, 207, 1992.
25. Smirnov B.M., *Negative ions*, (New York: McGraw-Hill), 1982.
26. Zhelezniak M.B., Mnatsakanian A.Kh., Sizykh S.V., "Photoionization of Nitrogen-Oxygen Mixture by Gas Discharge Radiation" *High Temp.*, Vol. 20, 1982, p. 423.
27. Raizer Yu.P., *Gas Discharge Physics*, (Springer, Berlin), 1991.
28. Boeuf J.P., Lagmich Y., Callegary Th., Pichford L.C., UnferTh., "New insights in the physics of DBD plasma actuators for flow control ", AIAA Paper No. 2008-1376, 2008.
29. Soloviev, V.R., Krivtsov, V.M., "Surface barrier discharge modeling for aerodynamic applications" *J. Phys. D: Appl. Phys.*, Vol. 42, 2009.
30. Boeuf J.P., Lagmich Y., Unfer Th., Callegary Th., Pichford L.C., "Electrodynamic force in dielectric barrier discharge plasma actuators", *J. Phys. D: Appl. Phys.*, Vol. 40, 2007, pp. 652-662.

31. Enloe, C.L., McHarg, M.G., and McLaughlin, Th.E., "Time-correlated force production measurements of the dielectric barrier discharge plasma aerodynamic actuator", *J. Appl. Phys.*, Vol. 103, 2008, 073302.
32. Leonov, S., Opaitis, D., Miles, R., Soloviev, V., "Time-resolved measurements of plasma-induced momentum in air and nitrogen under dielectric barrier discharge actuation", *Physics of Plasmas*, Vol. 17, 2010, 113505.
33. Enloe, C.L., McHarg, M.G., Font G.I. and McLaughlin, Th.E., "Plasma-induced force and self-induced drag in the dielectric barrier discharge aerodynamic plasma actuator", AIAA Paper No. 2009-1622, Jan. 2009, Orlando Florida.
34. Font, G.I., Enloe, C.L., and McLaughlin, Th.E., "Effect of volumetric momentum addition on the total force production of a plasma actuator," AIAA Paper No. 2009-4285, June 2009, San Antonio Texas.
35. Jukes, T.N., Choi, K., Johnson, G.A., Scott S.J., "Characterization of surface plasma-induced wall flows through velocity and temperature measurements", *AIAA J.*, Vol. 44, 2006, pp. 764-771.
36. Thomas, F.O., Corke T.C., Iqbal M., Kozlov A., Schatzman D., "Optimization of Dielectric Barrier Discharge Plasma Actuators for Active Aerodynamic Flow Control", *AIAA J.*, Vol. 47, 2009, pp. 2169-2178.
37. Opaitis, D., Zaidi, S., Shneider, M., Miles, R., Likhanskii, A., Macheret. S., "Improving Thrust by Suppressing Charge Build-up in Pulsed DBD Plasma Actuators", AIAA Paper No. 2009-487, Jan. 2009, Orlando Florida.
38. Visbal, M.R., and Gaitonde, D.V., "Control of Vortical Flows Using Simulated Plasma Actuators," AIAA Paper No. 2006-505, Jan. 2006, Reno NV.
39. Roe, P.L., "Characteristic Based Schemes for the Euler Equations," *Annual Review of Fluid Mech.*, Vol. 18, 1986, pp. 337-365.
40. Chakravarthy, S.R., and Osher, S., "A New Class of High Accuracy TVD Schemes for Hyperbolic Conservation Laws," AIAA Paper No. 85-0363, 1985.
41. Weiss, J.M., Maruszewski, J.P., and Smith, W.A., "Implicit Solution of the Navier-Stokes Equations on Unstructured Meshes," AIAA Paper No. 97-2103, 1997.
42. Miller, D.S., and Wood, R.M., "Lee-Side Flow Over Delta Wings at Supersonic Speeds," NASA TP-2430, 1985.
43. McMillin, S.N., Thomas, J.L., and Murman, E.M., "Navier-Stokes and Euler Solutions for Lee-Side Flows Over Supersonic Delta Wings. A Correlation with Experiment," NASA TP-3035, 1990.
44. Kharitonov, A.M., Lutsky, A.E., and Shevchenko, A.M., "Investigations of Supersonic Vortex Cores Above and Behind of a Wing," 2nd European Conference for Aerospace Sciences (EUCASS), July 2-6, 2007, Brussels, Belgium.
45. Hall, M.G., "Vortex breakdown," *Ann Rev Fluid Mech.* Vol. 4, 1972, pp. 195-218.
46. Leibovich, S., "The structure of vortex breakdown," *Ann Rev Fluid Mech.*, Vol. 10, 1978, pp. 221-246.
47. Escudier, M.P., "Vortex breakdown: observations and explanations," *Prog. Aerospace Sci.*, Vol. 25, 1988, pp. 189-229.
48. Délyery, J.M. "Aspects of vortex breakdown," *Prog. Aerospace Sci.*, Vol. 30, 1994, pp.1-59.

49. Althaus, W., Brucker, C. and Weimer, M., "Breakdown of slender vortices," In *Fluid Vortices*, ed. Sheldon Green, Kluwer Academic Publisher, 1995, pp. 373-426.
50. Lucca-Negro, O. and O'Doherty, T., "Vortex breakdown: a review," *Progress in Energy and Combustion Science*, Vol. 27, 2001, pp. 431-481.
51. Mitchell, A.M. and Détery, J., "Research into vortex breakdown control," *Prog. Aerospace Sci.*, Vol. 37, 2001, pp. 385-418.
52. Gursul, I., Yang, H., and Deng, Q., "Control of vortex breakdown with leading-edge devices," AIAA Paper No. 94-1857, June 1994.
53. Gursul, I., Srinivas, S. and Batta, G., "Active control of vortex breakdown over a delta wing," *AIAA J.*, Vol. 33, No. 9, 1995, pp. 1743-1745.
54. Wahls, R.A., Vess, R.J. and Moskovitz C.A., "Experimental investigation of apex fence flaps on delta wings," *J. of Aircraft*, Vol. 23, No. 10, 1986, pp. 789-797.
55. Lamar, J.E., "Analysis and design of strake-wing configurations," *J. of Aircraft*, Vol. 17, No. 1, 1980, pp. 20-27.
56. Er-El, J. and Seginer, A., "Vortex trajectories and breakdown on wing-canard configurations," *J. of Aircraft*, Vol. 22, No. 8, 1985, pp. 641-648.
57. Er-El, J., "Effect of wing/canard interference on the loading of a delta wing," *J. of Aircraft*, Vol. 25, No. 1, 1988, pp. 18-24.
58. Tu, E.L., "Navier-Stokes simulation of a close-coupled canard-wing-body configuration," *J. of Aircraft*, Vol. 29, No. 5, 1992, pp. 830-838.
59. Tu, E.L., "Effect of canard deflection on close-coupled canard-wing-body aerodynamics," *J. of Aircraft*, Vol. 31, No. 1, 1994, pp. 138-145.
60. Tu, E.L., "Vortex-wing interaction of a close-coupled canard configuration," *J. of Aircraft*, Vol. 31, No. 2, 1994, pp. 314-321.
61. Hummel, D. and Oelker, H.C., "Low-speed characteristics for the wing-canard configuration of the international vortex flow experiment," *J. of Aircraft*, Vol. 31, No. 4, 1994, pp. 868-878.
62. Howard, R.M. and O'Leary, J.F., "Flowfield study of a close-coupled canard configuration of the international vortex flow experiment," *J. of Aircraft*, Vol. 31, No. 4, 1994, pp. 908-914.
63. Helin, H. and Watry, C.W., "Effects of trailing-edge jet entrainment on delta wing vortices," *AIAA J.*, Vol. 32, No.4, 1994, pp. 802-804.
64. Nawrocki, D., "Differential and vectored trailing-edge jet control of delta wing vortices," AIAA Paper No. 95-0008, Jan. 1995, Reno NV.
65. Shih, C. and Ding, Z., "Trailing-edge jet control of leading edge vortices of a delta wing," *AIAA J.*, Vol. 34, No.7, 1996, pp. 1447-1456.
66. Vorobieff, P.V. and Rockwell, D.O., "Vortex breakdown on pitching delta wing: control by intermittent trailing-edge," *AIAA J.*, Vol. 36, No. 4, 1998, pp. 585-589.
67. Mitchell, A.M., Molton, P., Barberis, D. and Détery, J., "Control of leading-edge vortex breakdown by trailing-edge injection," *J. of Aircraft*, Vol. 39, No. 2, 2002, pp. 221-226.
68. Wang, J.J., Li, Q.S. and Liu, J.Y., "Effects of a vectored trailing edge jet on delta wing vortex breakdown," *Experiments in Fluids*, Vol. 34, 2003, pp. 651-654.

69. Parmenter, K. and Rockwell, D., "Transient response of leading-edge vortices to localized suction," *AIAA J.*, Vol. 28, No. 6, 1990, pp. 1131-1132.
70. Miller, S. and Gile, B., "The effects of blowing on delta wing vortices during dynamic pitching at high angles of attack," AIAA Paper No. 92-0407, Jan. 1992, Reno NV.
71. Kuo, C.H., Lu, N.Y. and Lin, D.C., "Evolution of vertical structure over delta wing with transient along-core blowing," *AIAA J.*, Vol. 35, No. 4, 1997, pp. 617-624.
72. Kuo, C.H. and Lu, N.Y., "Unsteady vortex structure over delta-wing subject to transient along-core blowing," *AIAA J.*, Vol. 36, No. 9, 1998, pp. 1658-1664.
73. Mitchell, A.M., Barberis, D., Molton, P. and Détery, J., "Oscillation of vortex breakdown location and blowing control of the time averaged location," *AIAA J.*, Vol. 38, No. 5, 2000, pp. 793-803.
74. Dixon, C. J., "Lift augmentation by lateral blowing over a lifting surface," AIAA Paper No. 69-193, Feb. 1969, Atlanta GA.
75. Rao, D.M., "Recent studies of slot-blowing techniques for vortex breakdown control on slender configurations," Fluid Dynamics of High Angle of Attack, IUTAM Symposium Tokyo/Japan, Session T.3: Flow Control, 1992, pp. 237-253.
76. Bradley, R.G. and Wray, W.O., "A conceptual study of leading-edge vortex enhancement by blowing," *J. of Aircraft*, Vol. 11, No. 1, 1974, pp. 33-38.
77. Cui, Y.D., Lim, T.T. and Tsai H.M. , "Control of vortex breakdown over a delta wing using forebody slot blowing," *AIAA J.*, Vol. 45, No. 1, 2007.
78. Budovsky A.D., Zanin B.Yu., Zverkov I.D., Kozlov V.V., Maslov A.A., and Postnikov B.V., Sidorenko A.A., "Plasma Control of Vortex Flow on Delta-Wing at High Angles of Attack," International Conference on Methods of Aerophysical Research (ICMAR). Novosibirsk, Russia. 2008.

Publications

- P1. Shalaev, V., Fedorov, A., Malmuth, N., and Shalaev, I., "Mechanism of Forebody Nose Vortex Symmetry Breaking Relevant Plasma Flow Control," AIAA Paper No. 2004-0842, Reno NV, Jan. 2004.
- P2. Maslov, A.A., Zanin, B.Yu., Sidorenko, A.A., Fomichev, V.P., Postnikov, B.V., and Malmuth, N., "Plasma Control of Separated Flow Asymmetry on a Cone at High Angle of Attack," AIAA Paper No. 2004-0843, Reno NV, Jan. 2004.
- P3. Malmuth, N., Krivtsov, V., and Soloviev, V., "Quick, Gridless Estimations of MHD Effects on Hypersonic Inlet Ramp Shocks," AIAA Paper No. 2004-0862, Reno NV, Jan. 2004.
- P4. Zhakharov, S.B., Fedorov, A.V., and Malmuth, N.D., "Modeling of Forebody Nose Symmetry Breaking Using Conical Navier-Stokes Solutions," AIAA Paper No. 2006-1257, Reno NV, Jan. 2006.
- P5. Malmuth, N., "Theoretical Aerodynamics in Today's Real World, Opportunities and Challenges," Julian D. Cole Lecture, *AIAA J.*, **44**, No.7, 2006, pp. 1377-1392

- P6. Malmuth, N.D., Zhakharov, S.B., and Fedorov, A.V., "Conical Navier-Stokes Modeling of Forebody Vortex Symmetry Plasma Control," AIAA Paper No. 2007-0219, Reno NV, Jan. 2007.
- P7. Soloviev, V.R., Krivtsov, V.M., Konchakov, A.M., and Malmuth, N.D., "Surface Barrier Discharge Simulation in Air for Constant Applied Voltage", AIAA Paper No. 2008-1378, Reno NV, Jan. 2008.
- P8. Soloviev V.R., Konchakov A.M., Krivtsov V.M., Aleksandrov N.L., "Numerical Simulation of a Surface Barrier Discharge in Air", *Plasma Physics Reports*, **34**, No.7, 2008, , pp.594-608.
- P9. Soloviev, V.R., Krivtsov, "Features of a Surface Barrier Discharge Modeling", AIAA Paper No. 2009-0842, Orlando FL, Jan. 2009.
- P10. Fedorov, A.V., and Soudakov, V.G., "Modeling of Plasma Flow Control over a High-Speed Delta Wing," AIAA Paper No. 2009-0699, Orlando FL, Jan. 2009.
- P11. Soloviev, V.R., Krivtsov, V.M., "Surface barrier discharge modeling for aerodynamic applications", *J. Phys. D: Appl. Phys.*, **42**, 2009, 125208(13pp).
- P12. Soloviev, V.R., Krivtsov V.M., "Phenomenological Model of the Body Force Induced by Surface Dielectric Barrier Discharge", AIAA Paper No. 2011-xxxx, Orlando FL, Jan. 4-7 2011.
- P13. Fedorov, A.V., Krivtsov, V.M., Soloviev, V.R., and Soudakov, V.G., "Modeling of Aerodynamic Forcing Induced by Surface Dielectric Barrier Discharge," AIAA Paper No. 2011-xxxx, Orlando FL, Jan. 4-7 2011.